Ocean Engineering 328 (2025) 121061

Contents lists available at ScienceDirect

Ocean Engineering

journal homepage: www.elsevier.com/locate/oceaneng

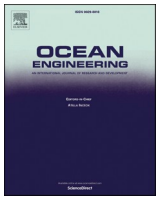

Research paper

Micromechanical analysis of local scour behaviors around circular piles in granular soil under steady flows with SPH-DEM

Yu Peng , Zhen-Yu Yin *

Department of Civil and Environmental Engineering, The Hong Kong Polytechnic University, Hung Hom, Kowloon, Hong Kong, China

ARTICLE INFO

Keywords:
Scour behavior
Micromechanics
Granular soil
Coupled SPH-DEM
Pile-water-soil interaction

ABSTRACT

The micro-mechanism of local scour around circular piles in granular soil under steady flows remains unclear. This study investigates local scour around circular piles with the coupled Smoothed Particle Hydrodynamics-Discrete Element Method (SPH-DEM) for the first time, taking the effects of scour lengths and flow velocities into consideration. The granular soil and piles are modeled using DEM elements, while the water is modeled using SPH elements. The flow regularity and scour holes in numerical simulations are compared with those in experiments, while detailed pile-water-soil interactions are analyzed. The findings demonstrate that the flow behaviors evolve with the development of scour holes. Large deformation and turbulent flow occurrences surrounding piles are successfully simulated using the SPH-DEM approach and their relationships to scour lengths are discovered. Besides, relationships between local flow direction, vortexes, and soil erosion are established by analyzing the streamlines and fluid force on particles. Furthermore, detailed investigations of particle transportation and scour holes under both flow and flow-stop conditions lead to an identification of conclusive modes of soil erosion around piles. This study provides novel insights into local scour behaviors around pile foundations in granular soil.

1. Introduction

The rapid global population growth and industrialization have created an unprecedented demand for resources, energy, and habitable spaces, prompting the expansion of infrastructure into riverine and marine environments (Chiew and Melville, 1987; Jia et al., 2023; Zandi et al., 2024). In these riverine and marine environments, circular pile foundations are extensively employed to support diverse engineering buildings and structures including bridges, offshore platforms, wind turbines, and harbor structures in granular soil (Feng et al., 2024; Wang et al., 2023; Xu et al., 2019a). In recent decades, one of the most critical challenges associated with pile foundations in such hydraulic environments is the issue of local scour caused by flowing waters (Wang et al., 2024a). Local scour around piles not only damages the riverbed or seabed but also significantly reduces the bearing capacity of the piles, which can even lead to the catastrophic failure of buildings and structures supported by these pile foundations in granular soil (Jiang et al., 2024; Kitsikoudis et al., 2017; Roulund et al., 2005). By understanding how steady flow affects scour around circular piles, engineers can optimize pile design and implement effective scour protection measures, thereby enhancing structural longevity and safety (Liang et al., 2019; Najafzadeh et al., 2025; Yang et al., 2020). Researching scour around circular piles also helps minimize environmental impacts by improving predictions of sediment transport and seabed changes, enabling cost-effective design strategies and ensuring compliance with regulations governing coastal and marine construction (Du and Liang, 2019; Liang et al., 2019; Tafarojnoruz and Lauria, 2020). Therefore, understanding and predicting local scour behaviors around piles in granular soil is of paramount importance for pile foundation engineering in riverine and marine environments.

Over the past several decades, extensive experiments and tests (Du et al., 2023a, 2023b; Yang et al., 2020; Yao et al., 2018) have been conducted to investigate the local scour behaviors around piles in flowing waters. These investigations have revealed that the local scour processes around piles in flowing water entail complex interactions between the piles, water flow, and soil particles. In the early days, experimental studies, finished in hydraulic flumes, mainly focused on examining the basic scour characteristics and developed empirical formulas or advanced to predict scour depth in granular soil (Chiew and Melville, 1987; Melville and Sutherland, 1988). These experiment and

* Corresponding author.
E-mail address: zhenyu.yin@polyu.edu.hk (Z.-Y. Yin).

https://doi.org/10.1016/j.oceaneng.2025.121061
Received 29 December 2024; Received in revised form 21 March 2025; Accepted 22 March 2025
Available online 2 April 2025

test studies have revealed that numerous factors such as pile diameter, sediment grain size, flow velocity, and water depth play a crucial role in determining the scour width and depths (Chiew and Melville, 1987; Chiew, 1990; Chow and Herbich, 1978). With advancements in experimental techniques, methods like laser Doppler velocimetry and particle image velocimetry have been utilized to analyze the behavior of sediment and flow around piles with high precision (Roulund et al., 2005; Sumer et al., 1992). These subsequent experiments have delved deeper into the local scour behaviors, investigating aspects such as the temporal evolution of scour, the impact of multiple piles or intricate pile configurations, and the interactions between hydrodynamic forces and sediment transport (Kitsikoudis et al., 2017; Yang et al., 2020; Yao et al., 2018). Furthermore, by leveraging experimental and test data, researchers have employed advanced statistical analysis techniques, such as evolutionary algorithms and neuro-fuzzy approaches, to uncover more precise relationships between scour depth around piles and factors such as bed sediment, pile configuration, pile geometry, and approaching flow (Ahmadianfar et al., 2022; Amini Baghbadorani et al., 2017; Bateni and Jeng, 2007; Najafzadeh and Azamathulla, 2015; Najafzadeh and Sheikhpour, 2024). These experimental data and relevant statistical analyses have provided a wealth of insights, forming the basis for many current engineering practices and design guidelines (Gao et al., 2024; Najafzadeh and Sheikhpour, 2024; Sumer et al., 2001; Wang and Reese, 1988). Despite the valuable insights gained from these experimental studies, experimental research faces inherent limitations. These limitations include challenges in observing initial sediment erosion, understanding the complex interactions between turbulence and particles, and obtaining detailed evolution of scour holes without disturbance from monitoring instruments. Additionally, conducting local scour testing in a hydraulic flume is costly and time-consuming.

In response to these challenges in experimental studies, numerical simulations have emerged as a powerful tool to complement experimental research on local scour around piles (Roulund et al., 2002, 2005). Classical numerical methods, including different computational fluid dynamics (CFD) models, relying on Reynolds-averaged Navier--Stokes (RANS) equations and large eddy simulation (LES), have been extensively employed for simulating scour processes (Dutta et al., 2023; Liu et al., 2022; Tafarojnoruz and Lauria, 2020). These models can capture large-scale flow features and provide valuable insights into mean flow velocities, turbulence characteristics, and sediment transport rates (Dutta et al., 2023; Wang et al., 2022b). For example, RANS-based CFD models have been successfully applied to simulate the steady-state fluid flow around piles, enabling researchers to gain a better understanding of the velocity distribution, flow separation, and vortical structures that contribute to local scour formation (Ahmad et al., 2016; Roulund et al., 2005). Large Eddy Simulation (LES), in contrast, has been widely used to resolve transient turbulence features, providing a more detailed representation of turbulence dynamics, particularly in regions with high flow acceleration and recirculation zones (Tafarojnoruz and Lauria, 2020). LES has proved to be especially useful in studying the effects of flow turbulence on sediment transport and scour depth over time, offering insights into how eddies and turbulent vortices contribute to the erosion and deposition of sediment around piles (Dutta et al., 2023). Therefore, these classical CFD models, including RANS and LES, have proven to be invaluable tools for researchers seeking to understand the local scour around piles.

However, continuum-based numerical methods like CFD models face significant challenges in simulating fine-scale turbulent flows and intricate soil-water interactions (Das et al., 2014; Quezada et al., 2018; Roulund et al., 2005). While RANS-based CFD models have been extensively used to simulate flow dynamics around structures such as piles, they often struggle to resolve the fine-scale turbulence and discrete particle interactions that are crucial for accurately predicting sediment transport and local scour around structures (Quezada et al., 2018; Roulund et al., 2005). Besides, the assumption of a continuous sediment bed in CFD models severely limits their ability to simulate the complex, localized movements of individual sediment particles—key to understanding the scour process. Studies by Das et al. (2014) and Roulund et al. (2005) have demonstrated that while CFD models effectively simulate flow patterns and turbulence, they are less adept at capturing the micromechanical processes that drive sediment erosion and deposition. Moreover, the reliance on empirical sediment transport formulations, often based on semi-empirical relations like the Shields criterion or bed-load transport equations, not directly from basic physical relations in the CFD models, further complicates accurate scour prediction under varying conditions (Dutta et al., 2023).

In response to these challenges, particle-based methods such as the Smoothed Particle Hydrodynamics (SPH) and Discrete Element Method (DEM) have gained significant attention due to their ability to handle complex fluid dynamics and granular interactions. SPH, a mesh-free Lagrangian method, discretizes the fluid into particles, enabling the natural simulation of free-surface flows, large deformations, and turbulent conditions (Ng et al., 2020; Wu et al., 2016). It has been successfully applied in various fields, including coastal engineering, dam-break simulations, and multiphase flows (Bagheri et al., 2024; Monaghan, 2012). On the other hand, DEM excels in modeling the motion and interactions of individual sediment particles, providing a detailed analysis of granular soil evolution at the particle scale (Chen et al., 2018; Cundall and Strack, 1979; Peng et al., 2021). DEM has been widely used in geotechnical engineering to study particle deposition, inter-particle collisions, and granular flow dynamics (Guo and Curtis, 2015; Mao et al., 2023; Tavarez and Plesha, 2007). The coupled SPH-DEM approach, which integrates the strengths of both methods, has emerged as a promising solution for simulating fluid-particle interactions. Recent studies have demonstrated its potential to address challenges such as sediment transport, scour development, and granular-fluid interactions (Su et al., 2024; Wu et al., 2016; Xu et al., 2019b). For instance, Wu et al. (2016) successfully applied SPH-DEM to model sediment transport in open-channel flows, highlighting its ability to capture particle-scale dynamics. Similarly, Xu et al. (2019b) utilized the coupled approach to study submerged granular collapse, demonstrating its superiority over traditional continuum-based methods in capturing detailed particle-fluid interactions. Despite these advancements, the application of SPH-DEM to local scour behaviors around piles remains unexplored. This study aims to bridge this gap by applying the coupled SPH-DEM approach for the first time to investigate the local scour mechanisms around circular piles, offering new insights into the micromechanical behavior of sediment transport and scour development.

Therefore, this research explores the mechanisms of local scour around piles in steady-flow water, utilizing a series of coupled SPH-DEM simulations for the first time. Detailed water flow and soil erosion behaviors in pile-water-soil interactions are revealed from the particle scale to the macro scale. This study begins by determining the evolution stages of local soil erosion and the main turbulent flow zone, then examines detailed flow velocity distributions and streamline distributions around piles. Subsequently, after a quantitative analysis of fluid forces on particles, particle transportation characteristics, and dimensions of scour holes, several scour modes have been concluded. The findings offer new insights into local scour behaviors around piles, potentially aiding in the design of pile foundations in riverine and marine environments.

2. Coupled SPH-DEM approach

2.1. SPH fundamentals for water phase

The Smoothed Particle Hydrodynamics (SPH) method is a fully Lagrangian and meshless approach that provides considerable benefits in simulating free-surface flows and large deformation behaviors, especially for fluid under turbulent conditions (He et al., 2018; Wu et al., 2016). In SPH, the fluid is represented by a finite set of irregularly

spaced nodes known as SPH particles (elements), each carrying essential properties such as mass, density, velocity, position, and pressure. These SPH particles act as interpolation points for integrating the Navier-Stokes equations that control fluid flow. Physically, these points can be perceived as small fluid parcels interacting with their neighbors through pressure and viscous forces (Potapov et al., 2001).

Each SPH particle i at the position $\mathbf{r}_i$ interacts to varying degrees with its surrounding particle j at the position $\mathbf{r}_j$ (Fig. 1), influenced by the distance $|\mathbf{r}_i - \mathbf{r}_j|$ between them and the value of the kernel function $W(\mathbf{r}_i - \mathbf{r}_j, h)$. This kernel function depends on the smoothing length h, which is of the order of the initial spacing between SPH particles. A property $f(\mathbf{r}_i)$ for an SPH particle i in a continuous domain is described using the following integral approximation with a weighted kernel function W:

$$f(\mathbf{r}_i) = \int f(\mathbf{r}_j) W(\mathbf{r}_i - \mathbf{r}_j, h) d\mathbf{r}_j \tag{1}$$

Where the smoothing length h in SPH simulations defines the spatial range over which particle properties, such as density and pressure, are averaged or smoothed. It controls the resolution of the simulation, affecting how particles influence each other and the accuracy of the physical representation.

The selection of kernel function is largely determined by the specific flow conditions (Bagheri et al., 2024; Cleary, 1998). Three widely used kernel functions Cubic, Quintic, and Wendland have been tested in the SPH-DEM simulations. Consistent with previous studies (Monaghan, 2012; Potapov et al., 2001; Ye et al., 2019), the Wendland kernel has demonstrated a superior ability to capture turbulence and complex flow behaviors compared to the Cubic and Quintic kernels. Given the complex turbulent vortices and drastic surface flow deformation observed around the pile in experiments, the Wendland kernel was selected for its robustness in simulating these phenomena. The Wendland kernel is defined as follows:

$$W_{ij} = W(\mathbf{r}_{ij}, h) = W(\mathbf{r}_i - \mathbf{r}_j, h) = \begin{cases} \frac{1}{256\pi h^3} \times (1 + 2x)(2 - x) & 0 \le x < 2 \\ 0 & x \ge 2 \end{cases} \tag{2}$$

The parameter x used in the kernel function equations is defined as:

$$x = \frac{d_{\text{sph}}}{h} \tag{3}$$

Where d_{sph} is the distance between two neighboring SPH particles i and j. In our study, the Ansys software is utilized to simulate fluid flows using the SPH method. Ansys harnesses the parallel computing capabilities of Graphics Processing Units (GPUs) to speed up calculations, making it highly effective for large-scale fluid dynamics simulations.

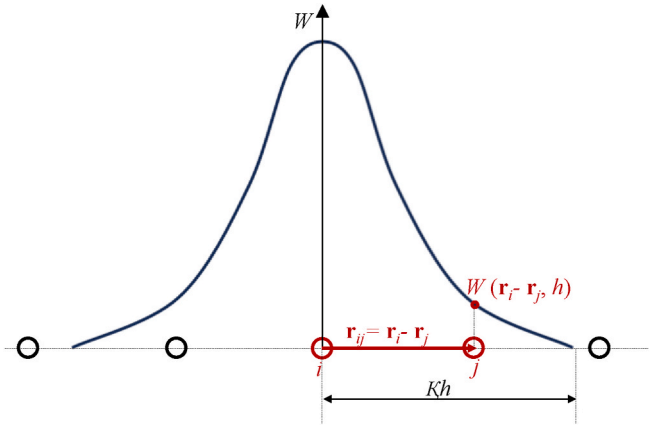

Fig. 1. Illustration of the kernel function in relation to the distance between fluid particle i and j ($K = 2.0$ according to Cleary, 1998, Kh is the cutoff radius).

Currently, the Weakly Compressible SPH (WCSPH) method, is suitable for compressible flows with a sufficiently low Mach number of less than 0.1 (corresponding to an almost incompressible fluid). In the SPH formulation (Monaghan, 1992, 2000), the continuity equation describes how the density of an SPH particle at position $\mathbf{r}_i$ evolves over time, as defined below:

$$\frac{d\rho_i}{dt} = \sum_j m_j (\mathbf{v}_i - \mathbf{v}_j) \cdot \nabla W_{ij} \tag{4}$$

Where ρ_i is the density of the fluid particle i; m_j is the mass of the neighboring fluid particle j; $\mathbf{v}_i$ and $\mathbf{v}_j$ are the velocities of the fluid particles i and j, respectively.

The equations of motion for fluid particles are derived from the Navier-Stokes equations. It is integrated explicitly to give the velocity variation over time, defined as follows:

$$\frac{d\mathbf{v}_i}{dt} = \mathbf{a}_{P,i} + \mathbf{a}_{visc,i} + \mathbf{a}_{m,i} + \mathbf{a}_{s \to w,i} \tag{5}$$

$$\mathbf{a}_{P,i} = -\sum_j m_j \left(\frac{P_i}{\rho_i^2} + \frac{P_j}{\rho_j^2} \right) \nabla W_{ij} \tag{6}$$

$$\mathbf{a}_{m,i} = \mathbf{g} \tag{7}$$

Where $\mathbf{v}_i$ is the velocity of the SPH fluid particle i; $\mathbf{a}_{P,i}$ is the SPH fluid particle acceleration due to pressure forces; $\mathbf{a}_{visc,i}$ is the SPH particle acceleration due to viscous forces; $\mathbf{a}_{m,i}$ is the SPH fluid particle acceleration due to body forces; $\mathbf{a}_{s \to w,i}$ is the acceleration due to the interaction of solid particles; m_j is the mass of the neighboring fluid particles j; P_i and P_j are the pressure values corresponding to the positions of the fluid particles i and j, respectively; ρ_i and ρ_j are the density of the fluid particles i, j, respectively; $\mathbf{g}$ is the gravitational acceleration vector.

To consider the fast turbulent flow in SPH simulations, particle acceleration due to viscous forces is calculated by the Cleary approximation (Cleary, 1998), defined as follows:

$$\mathbf{a}_{visc,i} = \sum_j \alpha m_j \left(\frac{4\mu_i \mu_j (\mathbf{r}_i - \mathbf{r}_j) \nabla W_{ij}}{\rho_i \rho_j \left(\mu_i + \mu_j \right) \left((\mathbf{r}_i - \mathbf{r}_j)^2 + \eta^2 \right)} \right) (\mathbf{v}_i - \mathbf{v}_j) \tag{8}$$

$$\eta = f_{\min} d_{\text{ini}} \tag{9}$$

Where μ_i and μ_j are the dynamic viscosity values of the fluid corresponding to positions $\mathbf{r}_i$ and $\mathbf{r}_j$; α is a parameter with the value of 4.96333; η is a small value that prevents division by zero; $f_{\min}$ is a method parameter with the value of 0.01; d_{ini} is the initial SPH particles spacing.

An equation of state proposed for water to compute the relation between pressure and density is defined as follows:

$$P_i = P_{\text{bg}} + \frac{c_0^2 \rho_0}{\gamma} \left[\left(\frac{\rho_i}{\rho_0} \right)^{\gamma} - 1 \right] \tag{10}$$

Where P_i is the pressure of the particle i; P_{bg} is the background pressure; ρ_i is the local fluid density; ρ_0 is the initial fluid density; c_0 is the material speed of sound defined by sound speed, and could be calculated using the hydrostatic pressure as a reference, employing the formula $10\sqrt{gh}$; γ is a dimensionless value defining the material stiffness with the value of 7.

In this Weakly Compressible SPH (WCSPH) simulation, corrections and filters have been used to modify the pressure and velocity of the fluid. The density field calculation is critical since the pressure is directly coupled to the density using the equation of state. The inclusion of the density correction algorithm notably improves pressure distributions,

the density correction follows the well-known “Shepard" interpolation in the SPH literature (Colagrossi and Landrini, 2003), normally expressed as:

$$\rho_i^{new} = \frac{W_{ij}}{\sum_j \frac{W_{ij}}{\rho_j}} \tag{11}$$

Where ρ_i^{new} is the corrected density.

The corrected density ρ_i^{new} provided by the Shepard filter is a quick and simple correction to the density field applied every N_c timestep. An additional check is performed to limit the density values to an expected range. Two additional parameters, $f_{\rho,\min}$ and $f_{\rho,\max}$ provide the maximum negative and positive deviations from the initial density values allowed after the density correction. Therefore, these two parameters define the limiting values for the density of the SPH particles, according to:

$$\rho_i^{\min} = \max\left(\rho_i^{new}, \left(1 - f_{\rho,\min}\right)\rho_0\right) \tag{12}$$

$$\rho_i^{\max} = \min\left(\rho_i^{new}, \left(1 + f_{\rho,\max}\right)\rho_0\right) \tag{13}$$

Where ρ_0 is the initial fluid density; the values of 0.01 and 0.03 are the limits of $f_{\rho,\min}$ and $f_{\rho,\max}$, respectively.

The velocity field modification is achieved with the XSPH correction method (Monaghan, 1989). To consider the turbulence state of fast flow, the Large Eddy Simulation (LES), proposed by Violeau and Issa (2007) is adopted to replace the viscosity in the viscous acceleration term, as the sum of molecular viscosity and the turbulent viscosity (Violeau and Issa, 2007).

2.2. DEM fundamentals for soil phase and piles

The Discrete Element Method (DEM) is extensively documented in the literature; therefore, this section only introduces the basic contact law used in DEM. In DEM, the contact forces and torques between particles are computed while the positions and velocities are updated accordingly (Jensen et al., 2001b; Wensrich and Katterfeld, 2012; Xu et al., 2019b). Within the DEM framework, each particle k is treated as a rigid body characterized by its position $\mathbf{r}_k$ and radius r_k. A collision between two solid particles, k_1 and k_2, is identified when their separation distance d satisfies the condition of $d = |\mathbf{r}_{k_1} - \mathbf{r}_{k_2}| < r_{k_1} + r_{k_2}$. Based on previous research (Su et al., 2024; Ting et al., 1989), the contact forces $\mathbf{F}_k^{\text{cont}}$ on solid particle k can be defined as follows:

$$\mathbf{F}_k^{\text{cont}} = \mathbf{F}_k^n + \mathbf{F}_k^t \tag{14}$$

$$\mathbf{F}_k^n = K_n(r_{k_1} + r_{k_2} - d)\frac{\mathbf{r}_{k_1} - \mathbf{r}_{k_2}}{|\mathbf{r}_{k_1} - \mathbf{r}_{k_2}|} \tag{15}$$

$$\mathbf{F}_k^t = -K_t(\mathbf{v}_{k_1} - \mathbf{v}_{k_2})\left(1 - \frac{\mathbf{r}_{k_1} - \mathbf{r}_{k_2}}{|\mathbf{r}_{k_1} - \mathbf{r}_{k_2}|}\right) \tag{16}$$

$$\mathbf{T}_k = \mathbf{r}_k \times \mathbf{F}_k^{\text{cont}} + K_r \Delta\boldsymbol{\omega}^t \tag{17}$$

Where $\mathbf{F}_k^n$, $\mathbf{F}_k^t$ are the normal and tangential contact forces, respectively, and $\mathbf{T}_k$ is the torque on solid particle k. Here, K_n is the normal stiffness coefficient related to the elastic modulus, K_t is the tangential stiffness coefficient associated with Poisson’s ratio, and K_r is the rotational stiffness coefficient; $\mathbf{r}_k$ is the position vector from the center of mass of particle k to the contact point; The term $\Delta\boldsymbol{\omega}^t$ represents the increment in the rotation angle between particles.

The motion of the solid particles is governed by Newton’s second law. After considering the subsequent solid-fluid coupling, the translational and rotational equations of motion for a single soil particle k are expressed as:

$$m_k\frac{d\mathbf{v}_k}{dt} = \sum \mathbf{F}_k^{\text{cont}} + \sum \mathbf{F}_{w\to s,k} + m_k\mathbf{g} \tag{18}$$

$$I_k\frac{d\boldsymbol{\omega}_k}{dt} = \sum \mathbf{T}_k + \mathbf{T}_{w\to s,k} \tag{19}$$

Where m_k is the mass of the particle k; $\mathbf{v}_k$ is the velocity of the particle k; $\mathbf{F}_k^{\text{cont}}$ is the contact force exerted by neighboring solid particles or boundaries; $\sum \mathbf{F}_{w\to s,k}$ is the fluid force from surrounding water particles during solid-fluid coupling; I_k stands for the moment of inertia; $\boldsymbol{\omega}_k$ is the rotational velocity of the particle, and $\mathbf{T}_k$ represents the torque resulting from the contact force; $\mathbf{T}_{w\to s,k}$ is the torque from surrounding water particles during solid-fluid coupling.

2.3. Coupling of SPH-DEM

The SPH-DEM coupling approach is available to deal with solid-fluid interactions effectively. This is achieved by simulating fluid dynamics with the SPH method while modeling the behavior of discrete solid particles with the DEM method. When combined, this coupling approach allows for capturing the complex dynamics of solid-fluid interactions, particularly where fluid flow influences the movement and behavior of solid particles (Robinson et al., 2014; Wu et al., 2016). In the SPH-DEM coupling simulations, the SPH particles are initially configured in a regular arrangement (see Fig. 2). The solid particles (DEM particles) are much larger than the inter-particle spacing of fluid SPH particles. The solid-fluid interaction is achieved by placing SPH particles in the interior of the solid particles. These interior SPH particles are assigned artificial properties—mass, density, and velocity—initially matching those of the surrounding fluid particles, evolving in time in the same manner as the surrounding fluid SPH particles. Besides, the interior SPH particles move and rotate with the solid particle without influencing the density of the solid particle.

The algorithm of SPH-DEM coupling is achieved by solid-fluid no-slip conditions, meaning that the SPH particles move and rotate in sync with the solid DEM particles (Potapov et al., 2001). The detail of the no-slip boundary condition between DEM particles and SPH particles is shown in Fig. 3, considering a fluid SPH particle (shown as i) that is close enough to the interior SPH particle (shown as j). The line connecting these particles intersects the fluid-solid boundary at point O. The unit normal vector $\mathbf{n}$ to the fluid-solid boundary at point O can be constructed along with a line drawn tangent to the surface through point O. Since the angular and translational velocities of the solid particle are known, the velocity of the point O is also known. To ensure the no-slip condition, the fluid velocity at point O should be equal to the solid velocity at this point. To meet this condition to second-order accuracy, the artificial velocity of the interior SPH particle j, $\mathbf{v}_{j_{art}}$ is given a value based on the velocity gradient between points j and O:

$$\mathbf{v}_{j_{art}} = \mathbf{v}_o + \left(d_i / d_j\right)(\mathbf{v}_o - \mathbf{v}_i) \tag{20}$$

where $\mathbf{v}_o$ is the velocity of point O; $\mathbf{v}_i$ is the velocity of the fluid SPH particle i; d_i and d_j are the distances from the points i and j to the line tangent to the fluid–solid interface passing through the point O. To calculate the solid–fluid interaction forces in relevant equations, this velocity $\mathbf{v}_{j_{art}}$ is used instead of the actual velocity with which the particle is moving. The fluid–solid interaction force using $\mathbf{v}_{j_{art}}$ is also added with the opposite sign to the equation that governs the motion of the DEM particle.

The flow-induced torque describes the rotational effect exerted by the fluid on the solid particle. In this SPH-DEM coupling, the torque on a solid particle k is calculated as:

$$\mathbf{T}_{w\to s,k} = \sum_j \left(\mathbf{r}_{jk} \times \left(\left(\mathbf{v}_j - \mathbf{v}_k\right)\cdot\nabla W_{jk} m_j\right)\right) + \sum_j \left(\mathbf{r}_{jk} \times \left(\nabla p_j \cdot W_{jk} m_j\right)\right) \tag{21}$$

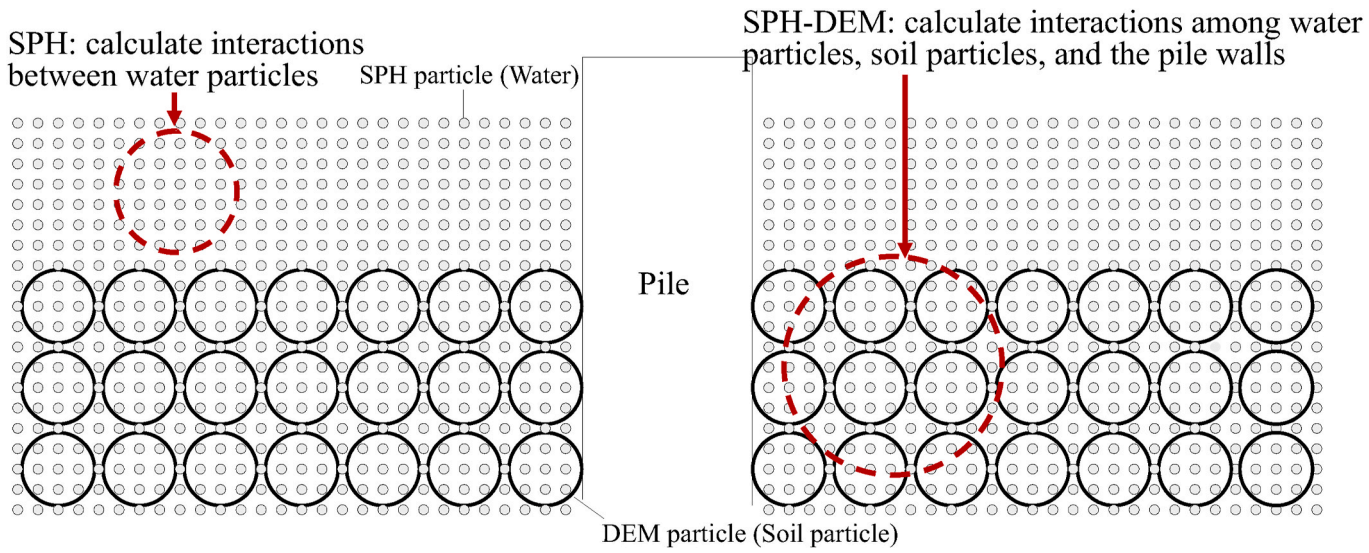

Fig. 2. Schematic diagram of SPH particles and DEM particles around piles in the SPH–DEM framework.

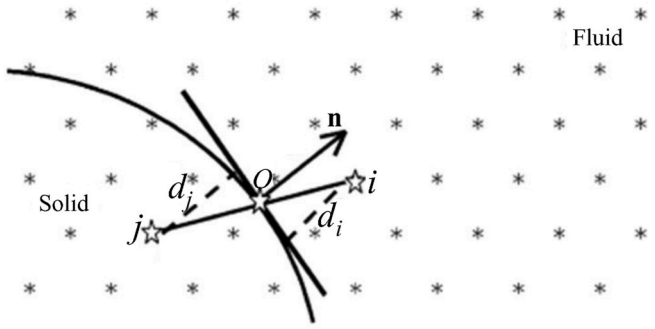

Fig. 3. Illustration of the no-slip boundary condition between DEM particle-SPH particle (modified from Potapov et al., 2001).

Where $\mathbf{r}_{jk}$ is the position vector from the solid particle k to the fluid particle j.

Granular motion alters the motion of fluid particles by solid-fluid interaction forces. The solid-fluid interaction force caused by the relative motion of solid granular and fluid particles includes the drag force and the pressure force from pressure gradients. For a solid particle k, the fluid force $\mathbf{F}_{w\to s,k}$ on it primarily consists of drag force $\mathbf{F}_{\text{drag},k}$ and pressure gradient force $\mathbf{F}_{\text{pressure},k}$ (Robinson et al., 2014), expressed as:

$$\mathbf{F}_{w\to s,k} = \mathbf{F}_{\text{drag},k} + \mathbf{F}_{\text{pressure},k} \tag{22}$$

$$\mathbf{F}_{\text{drag},k} = \frac{\beta V_k}{1-n_k}(\bar{\mathbf{v}}_w - \mathbf{v}_k) \tag{23}$$

$$\mathbf{F}_{\text{pressure},k} = V_k(-\nabla P + \nabla\cdot\boldsymbol{\tau}) \tag{24}$$

Where β is the interphase momentum, which can be obtained from two separate relations based on the local porosity (Ergun, 1952); V_k is the solid particle volume; n_k is the average local porosity; $\bar{\mathbf{v}}_w$ is the volume-averaged fluid velocity, typically obtained by interpolating SPH particle velocities in the vicinity of the solid particle; $\mathbf{v}_k$ is the velocity of the solid particle; ∇P is the pressure gradient; $\nabla\cdot\boldsymbol{\tau}$ is the divergence of the stress tensor (force due to viscous shear stresses in the fluid). The pressure gradient at solid particle k could be evaluated by using the Shepard corrected SPH interpolation, given in Robinson et al. (2014).

The fluid particle i will also receive reaction forces from all DEM particles within its support domain:

$$\mathbf{F}_{s\to w,i} = -\frac{m_i}{\rho_i}\sum_k \frac{W(|\mathbf{r}_{ki}|,h)}{\sum_j \frac{m_j}{\rho_j} W(|\mathbf{r}_{kj}|,h)}\mathbf{F}_{w\to s,k} \tag{25}$$

For more details about the above equations, please refer to the references Potapov et al. (2001); He et al. (2018). From a numerical implementation perspective, the SPH method simulates fluid motion, while DEM handles the granular motion. The drag force and pressure gradient force are computed based on the relative particle velocities and flow pressure distributions in the computational domain. These forces are incorporated into the SPH equations for fluid motion and the DEM equations for granular motion, ensuring that the two phases interact dynamically and influence each other's behavior.

As depicted in the SPH-DEM framework (Fig. 2), interactions occur not only between DEM and SPH particles but also between SPH particles and pile walls. The SPH-DEM approach uses DEM-style interactions with the walls of pile boundaries. When interacting with a boundary, the SPH particle experiences normal and tangential forces. Particles that are closer to the wall than the kernel radius have repulsive forces applied to them to prevent wall penetration. This normal repulsive force for the SPH-boundary contact is calculated using the linear spring-dashpot model, expressed as:

$$F_n = \begin{cases} K_{n,w}\times(0.5h - d_{wall}) + K_d v_n & d_{wall} \le 0.5h \\ 0 & d_{wall} \ge 0.5h \end{cases} \tag{26}$$

$$K_{n,w} = C_n \rho_i c_0^2 d_{ini} \tag{27}$$

where d_{wall} is the distance between the SPH particle and the wall; v_{n} is the normal velocity with respect to the wall; K_{d} is the viscous damping coefficient, which is a method parameter with a default value of 0; $K_{\text{n,w}}$ is the elastic coefficient; ρ_{i} is the SPH particle density; C_{n} is the Boundary Stiff. Factor, with the value of 0.5.

For simulating water turbulence around piles, a no-slip turbulent model is used to compute the tangential force between SPH particles and the wall boundary. The tangential force is expressed as:

$$F_\tau = \begin{cases} \rho_i (u^*) d_{ini}^2 & d_{wall} \le f_\tau d_{ini} \\ 0 & otherwise \end{cases} \tag{28}$$

where u^* is the shear velocity or friction velocity of an SPH particle in relation to the wall.

For this coupled SPH-DEM approach, both the SPH solver and the DEM solver march in time using the same timestep Δt, which is

computed as:

$$\Delta t = \min\left(\Delta t_{\mathrm{SPH}}, \Delta t_{\mathrm{DEM}}\right) \tag{29}$$

Where Δt_{SPH} and Δt_{DEM} is the timestep computed by the SPH solver and DEM solver, respectively. The timestep Δt_{DEM} is calculated based on the commonly used Rayleigh time (Li et al., 2005).

The timestep Δt_{SPH} is expressed as:

$$\Delta t_{SPH} = C_{ts}\frac{h}{c_0} \tag{30}$$

Where C_{ts} is a coefficient defined by timestep factor with the value of 0.25.

Recently, the SPH-DEM approach has been increasingly applied to flow-related issues due to its significant advantages in handling large deformations and turbulence (He et al., 2018; Sizkow and El Shamy, 2022; Su et al., 2024). However, there remains a lack of SPH-DEM simulations specifically focused on local scour issues around piles. This study focuses on the local scour behaviors around circular piles in non-cohesive granular soil using the coupled SPH-DEM method. Besides, the inability to effectively consider the effects of cohesive particles is widely recognized as an inherent limitation of common DEM-based models (Guo and Curtis, 2015; Wang et al., 2022a; Wu et al., 2016; Xu et al., 2019b). Consequently, the effect of cohesive particles is not considered in the current SPH-DEM model.

3. Simulations of local scour around piles

3.1. Brief introduction to the adopted experimental model tests

This research is based on the classical scour experiment from Roulund et al., (2005). The scour experiment was conducted in a current flume with sandy soil on the bottom. As shown in Fig. 4, the model circular pile with a diameter of 10 cm was positioned at the center position of the sandy soil. The representative particle sizes d_{15}, d_{50}, and d_{85} were around 0.13, 0.26, and 0.39 mm, respectively (Dey, 2014; Roulund et al., 2005). Here, d_{15}, d_{50}, and d_{85} represent the grain sizes at which 15 %, 50 %, and 85 % of the sand samples are finer, respectively. Among these, the d_{15} is regarded as the threshold particle size for erosion in studies of soil scour (Heibaum, 2004; Soroush et al., 2019). The water depth was 40 cm, and detailed velocities at different positions in the scour experiment were measured with a micro propeller. According to the vertical velocity profile at the experiment test in Fig. 5, the undisturbed mean flow velocity v_0 = 0.46 m/s. Consistent with previous studies (Chang et al., 2004; Guan et al., 2019; Petersen et al., 2015), scour depth (S) is a general term, defined as the vertical distance from the original undisturbed bed to the lowest point of the observed local region. The development of scour depth (S) at both the upstream side and the downstream side of the pile was monitored while the detailed

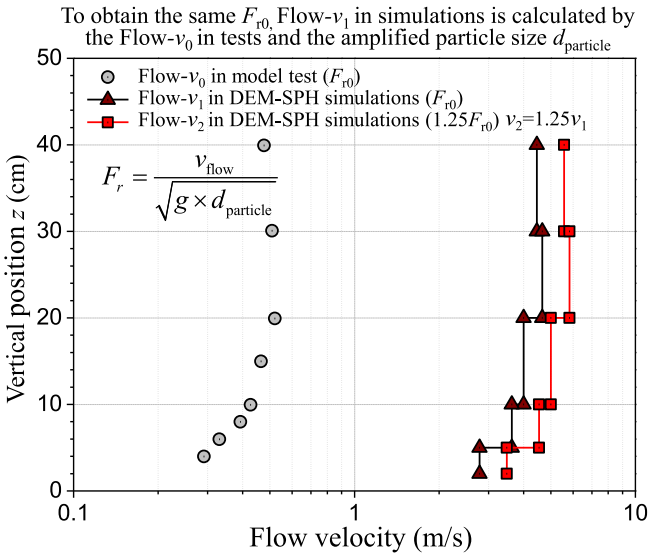

Fig. 5. Flow velocity profiles in experiment tests and numerical simulations.

dimensions of the scour hole were measured at the end of the scour test. Detailed information about the adopted model tests can be found in the study of Roulund et al. (2005).

3.2. SPH-DEM models in the local scour simulations

The selection of the SPH-DEM coupling approach in this study was motivated by the need for a suitable simulation of the complex interactions between fluid, sediment, and piles. While experimental studies and relevant statistical analyses offer valuable insights into local scour behavior and help predict scour depth around piles with relatively high accuracy, these studies face challenges such as the difficulty in observing fine-scale particle movement and the high costs/time requirements associated with conducting experiments in hydraulic flumes (Najafzadeh and Sheikhpour, 2024; Roulund et al., 2005). Classical numerical methods, such as CFD, can model large-scale flow characteristics but struggle to capture particle-scale sediment motion due to their reliance on continuum assumptions and empirical models, which can reduce accuracy. In contrast, the numerical SPH-DEM approach provides a particle-scale framework that could simulate detailed fluid-particle interactions and large deformations, offering a superior approach for studying the intricate behaviors of scouring around piles. For the feasibility validation of the coupled SPH-DEM approach to deal with scour problems, benchmark test-cases of dam break have been conducted by previous researchers (He et al., 2018; Su et al., 2024; Wu et al., 2016) with relatively satisfactory results.

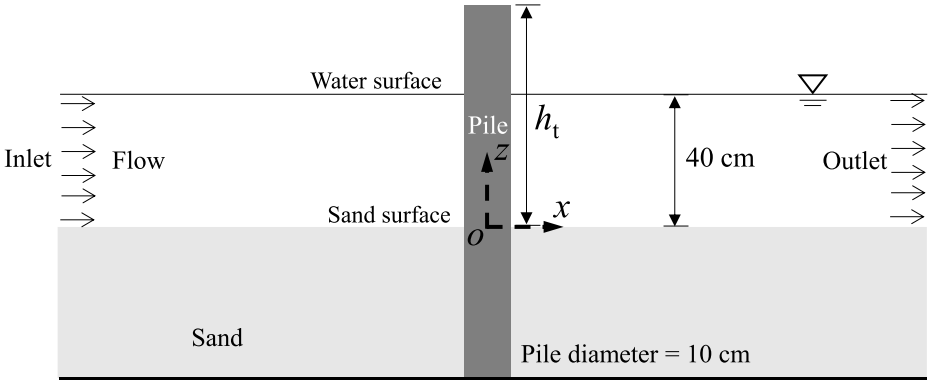

Fig. 4. Schematics of the adopted experimental model tests.

The pile diameter and water depth were the same as that in the experiment model tests. A view of the SPH–DEM numerical models is shown in Fig. 6. The soil in model tests was simulated with DEM particles. In line with prior studies (Peng and Yin, 2023), the Hertzian spring-dashpot model was used to calculate the normal contact force of solid particles, while the linear spring Coulomb limit model was used to calculate the tangential contact force in DEM-based simulations. To consider the particle angularity effect on particle contact behaviors, the linear spring rolling limit model proposed by Wensrich and Katterfeld (2012) was adopted in the DEM-based simulations. The ratio of tangential to normal stiffness of solid particles was set to 1.0 in the simulations. According to previous studies (Jensen et al., 2001b; Macaro et al., 2015), the particle size in DEM-based simulations focused on engineering issues should be much larger than that in experiment tests to obtain acceptable computational efficiency but without obvious particle scale effect. The threshold particle size d_{15} in the numerical model was 1.08 cm. The median particle diameter (d_{50}) in the numerical model was settled as 1.25 cm; thus, the ratio of pile diameter (D) to d_{50} was 8, which is sufficient to disregard the particle scale effect based on prior studies (Arroyo et al., 2011; Falagush et al., 2015; Gezgin et al., 2020). The sediment gradation was $\sigma_g = d_{85}/d_{50} = 1.5$, which is the same as that in the experiment model tests. The pile was modeled using wall elements within the DEM framework. The contact property between the pile and surrounding soil particles was governed by contact force models. Consistent with previous DEM-based studies on pile-soil interaction (Fahmi et al., 2024; Peng and Yin, 2023; Peng et al., 2022), the widely used Hertzian spring-dashpot model was employed to calculate the normal contact forces between solid particles, while the linear spring Coulomb limit model was utilized to determine the tangential contact forces in the simulations.

For computational efficiency, large-scale DEM-based studies inevitably use scaled particle sizes (Hu et al., 2019; Jensen et al., 2001b; Macaro et al., 2015; Peng and Yin, 2023). In such studies, where particle sizes are amplified, flow velocities are inevitably adjusted in nearly all DEM-based simulations to match the sediment dynamics observed in experiments (Ma et al., 2024; Su et al., 2024; Xu et al., 2019b; Yang et al., 2018; Zhang et al., 2023). This is commonly achieved by controlling key scour intensity parameters, such as the Froude number (F_r, in this study) or the Shields parameter (θ)(Hu et al., 2019; Liu et al., 2022; Su et al., 2024; Yang et al., 2018; Zhang et al., 2023). While particle size scaling may introduce some local differences in particle contacts between SPH-DEM simulations and experimental testing, controlling a key scour intensity parameter ensures that the overall sediment dynamics remain consistent and undistorted (Ma et al., 2024; Xu et al., 2019b; Yang et al., 2018, 2024). According to previous studies (Abou-Seida et al., 2009; Tan et al., 2020), the intensity of granular soil erosion in steady-flow water can be evaluated by the following equation:

$$F_r = \frac{v_{flow}}{\sqrt{g \times L}} \tag{31}$$

where F_r is the Froude number; v_{flow} is the flow velocity; g is the gravitational acceleration; L is the characteristic length, here is the threshold particle size ($d_{particle}$) in this numerical study.

Usually in local scour research focused on investigating the particle and pile factors, the intensity of granular soil erosion was settled at equal value (Du and Liang, 2019; Yang et al., 2020; Yao et al., 2018). Note that the particle size in DEM-based simulations was amplified from that in experiment tests. Thus, according to Eq. (31), to maintain the same soil erosion intensity as that in the adopted experiment model tests (F_{r0} = 9.02), the water flow velocity of a group of numerical simulations should be amplified. In numerical simulations, the flow velocity distribution along the water depth was simplified to five layers and the corresponding amplified velocity was the Flow-v_1, shown in Fig. 5. To further study the effect of scour intensity, another group of water flow velocity Flow-v_2 (v_2 = 1.25 v_1) in Fig. 5 was also adopted in the numerical simulations.

The water was simulated with SPH particles. According to previous research (Wu et al., 2016; Xu et al., 2019b), the density of water fluid was settled as 1000 kg/m^3 while the water viscosity was 0.001 Pa s. Key parameters for the SPH model are presented in Table 1. Since large-scale DEM-based simulations often face significant challenges in terms of computational efficiency, the selection of parameters aimed to minimize the number of particles (or elements) while still effectively capturing water-soil-pile interactions. The initial SPH particle spacing, d_{ini}, was set to 0.004 m, corresponding to a diameter slightly smaller than one-third of the d_{50} of solid particles, consistent with previous SPH-DEM simulations of water-soil-structure interactions (Jo et al., 2022). Based on previous studies (Bagheri et al., 2024; Wang et al., 2016), the smoothing length (h) is usually set around 1.25 times the initial SPH particle spacing. Therefore, similar to previous studies (Chaussonnet et al., 2015; Lin et al., 2015), the smoothing lengths were varied from 1.0 to 1.5 to conduct a sensitivity analysis, evaluating the interaction force, velocity field, and pressure field among particles to assess the accuracy and

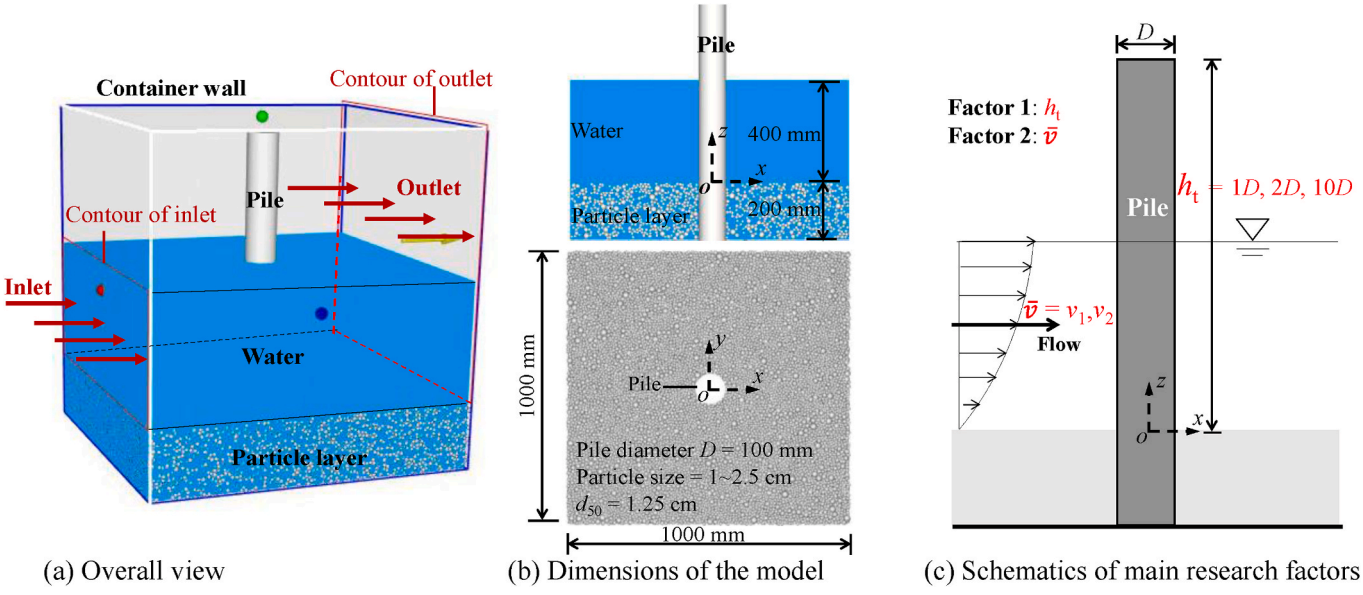

Fig. 6. A view of the SPH–DEM numerical models: (a) Overall view, (b) Dimensions of the model, and (c) Schematics of main research factors.

Table 1
Main parameter values in SPH-DEM simulations.

System	Parameters	Value	Unit
	Timestep	1.0×10^{-5}	s
Granular soil (Ball in DEM)	Density (ρ)	2650	kg/m^3
	Young's modulus (E)	1.0×10^6	N/m^2
	Friction coefficient (f)	0.5	\
	Restitution coefficient	0.30	\
	Rolling Resistance (RR)	0.10	\
	Poisson's ratio (υ)	0.30	\
	Gravitational acceleration (g)	9.8	m/s^2
	Median particle size (d_{50})	0.0125	m
Pile (Wall in DEM)	Elasticity modulus (E)	2.0×10^{11}	N/m^2
	Friction coefficient (f)	0.35	\
	Restitution coefficient	0.8	\
	Poisson ratio (υ)	0.3	\
Water (SPH)	Density (ρ)	1000	kg/m^3
	Viscosity	0.001	Pa•s
	Initial SPH particle spacing (d_{ini})	0.004	m
	Kernel function type	Wendland	\
	Kernel smooth length (h)	0.0044	m
	Sheilds parameter (θ)	0.55	\
	Critical shields parameter (θ_c)	0.05	\
	Friction velocity (u_*)	0.44	m/s
	Critical friction velocity (u_{*c})	0.073	m/s

stability of each configuration. The analysis revealed that setting the smoothing length between 1.1 and 1.3 times the initial SPH particle spacing achieves a relatively optimal balance of numerical accuracy, stability, and computational efficiency. To better capture flow details, a relatively small smoothing length of 1.1 times the initial particle spacing (d_{ini}) was ultimately selected as the optimal parameter for large-scale SPH-DEM simulations. Because the flow velocity in this numerical simulation was significantly amplified, the density correction was conducted every timestep ($N_c = 1$) to prevent excessive pressure diffusion, based on the study of Colagrossi and Landrini (2003). In this numerical study, the scour length (h_t) is defined as the length of piles above the initial water-soil interface. To study the effect of scour length, a variety of h_t including above-water and underwater conditions were considered ($h_t/D = 1$, 2 and 10).

3.3. Model validation

Similar to previous model validation in studies of the scour erosion around underwater structures (Hu et al., 2019; Ma et al., 2024; Roulund et al., 2005), the typical scour hole profile in the SPH-DEM simulations are compared with results from the classical experimental test and the simulation using EllipSys3D (Roulund et al., 2005). The soil erosion results in Fig. 7 indicate that the scour dimension in the SPH-DEM simulations basically coincides with that in the classical experiment test. Although the dimensionless scour depth (S/D) predicted by the SPH-DEM simulation is slightly shallower near the pile in comparison with the experimental results, it nonetheless exhibits improved accuracy over the earlier CFD-based numerical simulation by Roulund et al. (2005). Detailed results of the scour behaviors are analyzed in the following parts.

It is widely accepted that a multitude of grain factors, including grain size, shape, and void ratio have exhibited inevitable discrepancies between DEM-based simulations and geotechnical experimental tests (Bernhardt and Biscontin, 2016; Cil et al., 2020; Coetzee and Els, 2009; Jensen et al., 2001a). Thus, the specific values derived from DEM-based investigations may deviate somewhat from those obtained in experiments. Instead of aiming for exact numerical outcome values, concentrating on the insightful perspectives that provide micro mechanisms and trends in soil behaviors is more valuable. Additionally, similar to previous large-scale DEM-based studies on local scour erosion around structures (Ma et al., 2024; Yang et al., 2018; Zhang et al., 2023), the flow velocity in these DEM-SPH simulations does not correspond to the actual fluid velocity in experiments; therefore, the flow characteristics are primarily served as qualitative information to explain the local soil scour erosion around piles.

We acknowledge that large-scale DEM-SPH simulations are computationally demanding. For example, simulating flow around a single pile with a flow velocity of v_1 and $h_t = 10D$ requires approximately 50 h using 2 × RTX 4090 GPUs for parallel computation and a neighbor search algorithm to maintain acceptable computational efficiency. While DEM-SPH is less efficient for large-scale simulations compared to traditional methods like FEM or CFD-based methods, it offers distinct advantages in capturing complex scour processes without relying on empirical sediment transport equations (Russell and Wheeler, 1983; Violeau and Issa, 2007; Yang et al., 2024). The computational cost is primarily due to intensive particle interactions and fluid-solid coupling (Jo et al., 2022; Yang et al., 2024). Future optimizations, such as multi-GPU parallelization, adaptive time-stepping, improved neighbor-search algorithms, and optimized memory management, can further enhance computational efficiency.

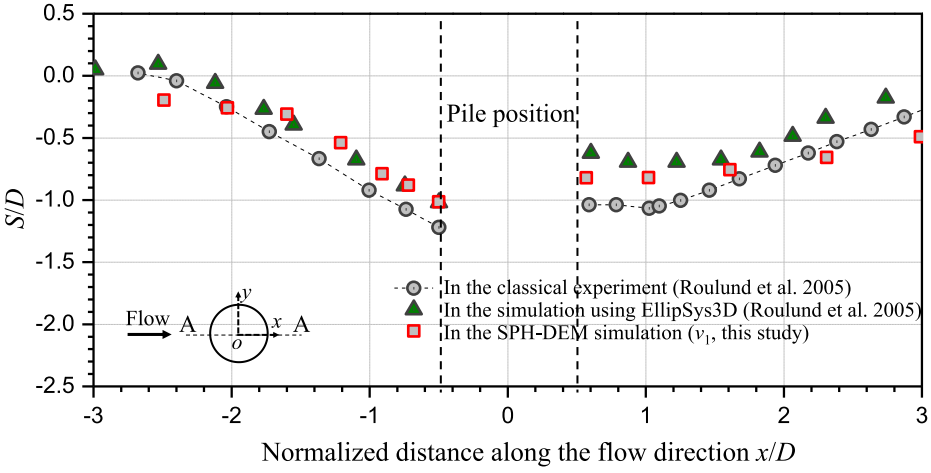

Fig. 7. Comparison of scour hole profiles along the flow direction (section A-A) in the classical experiment and numerical simulations (S: Local sour depth; D: Pile diameter).

4. Results and analysis

4.1. Overall view of the water flow and soil erosion around piles

The presence of pile foundations in flowing water significantly alters local hydrodynamics, sediment deposition, and particle transport around the piles (Kitsikoudis et al., 2017; Roulund et al., 2005). An overview of the typical flow velocity distribution around the piles on different water layers is shown in Fig. 8. The flow velocity noticeably increases on both sides of the piles due to the reduction in the cross-sectional area of water flow, while obvious turbulent flow and water-vacancy zones are observed behind the piles. Additionally, the flow-velocity decrease in the upstream zone of bottom flow layers (Fig. 8a) is unobvious compared to the obvious velocity decrease observed in the middle (Fig. 8b) and top flow layers (Fig. 8c), which should be attributed to the increase of the local discharge area after soil erosion around piles. To better illustrate the effect of soil erosion on water flow, the progressive development curves of lateral water flow velocity v_y in the test zone (Fig. 8) are shown in Fig. 9. In flow layers distant from the soil surfaces (h = 20~30 cm, 30~40 cm), the lateral water flow velocity v_y remains unaffected by scour time. However, in the flow layers closer to the soil surfaces (h = 0~10 cm, 10~20 cm), the lateral water flow velocity v_y decreases significantly with increased scour time, particularly within the initial 2 s. This phenomenon can be attributed to the rapid development of scour holes within the initial 2 s, which will be analyzed in detail in subsequent sections.

To provide a comprehensive understanding of local soil erosion development around circular piles and to identify different scour stages, an analysis of the progressive soil scouring loss around the piles has been conducted. Previous studies (Du and Liang, 2019; Roulund et al., 2005; Wang et al., 2024a) suggested that the radius of scour holes around piles is predominantly confined to a zone within 3D (where D is the pile diameter). Fig. 10 illustrates the percentage of mass loss around piles within an annular zone with an outer radius of 3D. The curves in Fig. 10 indicate that local soil erosion around piles can be divided into three stages: the fast scour stage, the progressive scour stage, and the stable flow stage, which is consistent with previous experimental studies (Du and Liang, 2019; Roulund et al., 2005). Detailed analysis of typical scour characteristics in these three stages will be presented in subsequent sections. When the scour length is small (h_t = 1D), the percentage of mass loss decreases slightly with increasing scour time. As the scour length h_t increases from 1D to 2D, the mass percentage decreases sharply, indicating a significant increase in soil particle loss due to local scour. However, when the scour length h_t increases substantially from 2D to 10D (transitioning from submerged to above-water conditions), the mass percentage decreases only slightly. The three curves under the same mean flow velocity v_1 demonstrate that the effect of scour length on soil erosions is pronounced when h_t is less than 2D. Additionally, an increase in flow velocity also significantly enhances soil erosion, as evidenced by the sharply decreased mass percentage under the mean flow velocity v_2. In conclusion, apart from the impact of flow velocity, an increase in scour length intensifies local soil erosion, particularly when the scour length is less than 2D.

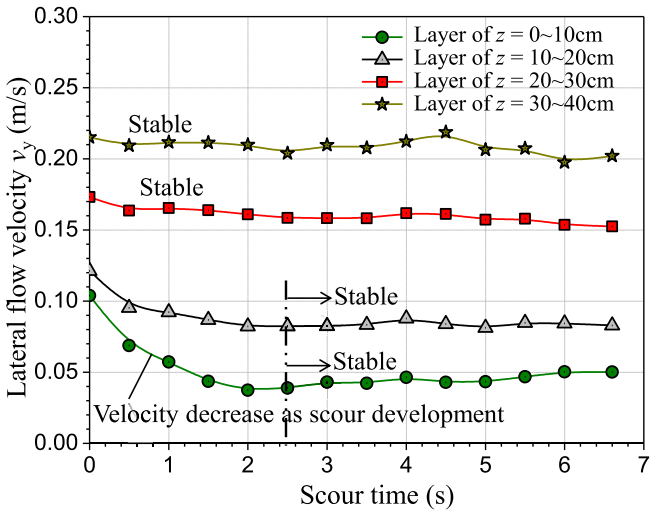

Fig. 9. Development curves of lateral flow velocity v_y around piles in different flow layers (h_t = 10D, v_1).

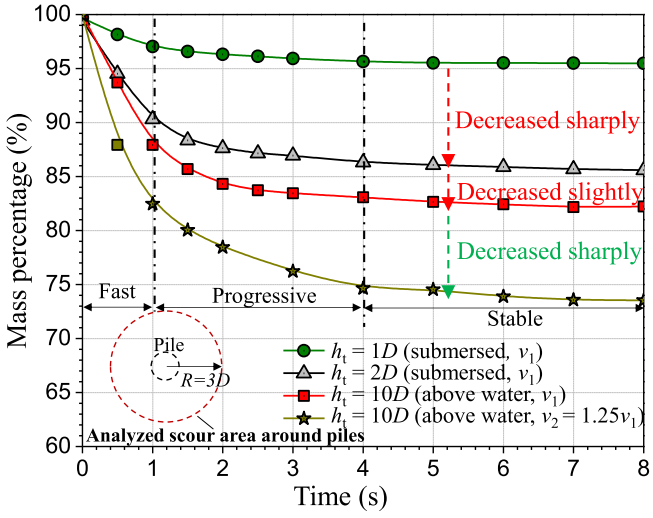

Fig. 10. Comparison of soil mass loss around piles due to soil erosion in different numerical cases.

It is worth noting that large-scale DEM-based studies involving the interaction between the water layer, underwater structures, and the soil layer often face significant challenges due to low computational efficiency (Hu et al., 2019; Ma et al., 2024; Peng and Yin, 2023). To obtain acceptable computational efficiency, the number of particles is typically minimized, resulting in a substantial sacrifice in fluid particle resolution

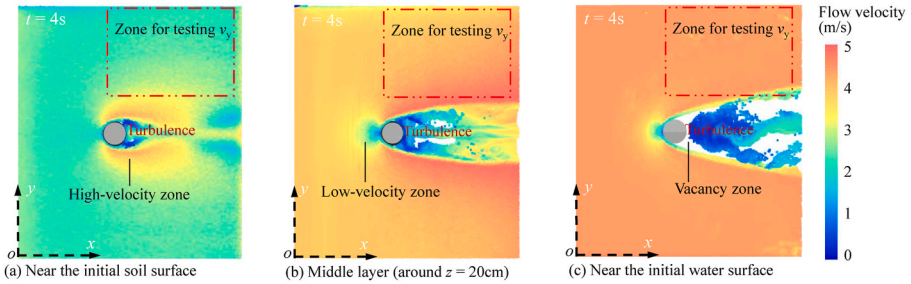

Fig. 8. Overview of typical flow velocity distributions around the pile (h_t = 10D, v_1) in different water layers: (a) Near the initial soil surface, (b) Middle layer (around z = 20 cm), and (c) Near the initial water surface.

and limiting research on the effects of fluid resolution in large-scale DEM simulations (Peng and Yin, 2023; Su et al., 2024; Zhang et al., 2023). However, it should be noted that increasing the resolution of fluid particle size, by reducing particle spacing and increasing the number of particles, can theoretically improve the accuracy of simulation results to some extent, as demonstrated in previous small-scale simulations (Manenti et al., 2012; Robinson et al., 2014; Ye et al., 2019).

4.2. Detailed fluid motion and fluid forces on soil particles

After a circular pile is constructed in steady-flow waters, the local flow patterns around the pile change significantly, characterized by large deformation and complex turbulence (Du et al., 2023a; Wang et al., 2024b). The local intensified flow induced by the obstruction of piles leads to the uplift of soil particles, contributing to the formation of scour holes around the piles (Beven and Germann, 2013; Chen and Bai, 2015). Typical vertical flow velocity distributions around piles during the stable flow stage ($t = 5$s) are depicted in Fig. 11. The images on the left display the vertical section along the flow direction (section A-A), while the right images show horizontal sections at different vertical positions corresponding to the left images. In all cases, there is a distinct downflow zone on the upstream side of the piles and a complex turbulent zone on the downstream side, consistent with the observations from the experimental study by Roulund et al. (2005).

Under a small scour length of $h_t = 2D$ (Fig. 11 a), a strong downflow is observed on the upstream side, while the turbulent zone on the downstream side is relatively small, as seen from the horizontal layer (H_0-H_0 plane) close to the water-soil interface. As the horizontal plane is elevated to a higher position, the length of the local upflow zone increases significantly. At the vertical position of the pile top (H_{2D}-H_{2D} plane in Fig. 11a), there is a small upflow zone on the upstream side and a wide unstable flow zone on the downstream side. When the scour length of the pile is sufficient to extend above the water surface (Fig. 11 b), the disturbance zone around the pile expands sharply. On the horizontal plane at mid-water depth (H_{2D}-H_{2D} plane) in Fig. 11b, two long downflow zones, accompanied by a strong central upflow zone, are observed on the downstream side. On the top horizontal layer (H_{4D}-H_{4D} plane) close to the water surface in Fig. 11b, a wide upflow zone is present on the upstream side, while water-vacancy zones emerge behind the pile due to the obstruction of piles, consistent with the previous experimental studies (Ozgoren, 2006; Roulund et al., 2005). Additionally, the high spray deformation on the upstream side and significant turbulence deformation on the downstream side are discovered on the vertical sections in Fig. 11b and c. Furthermore, higher spray and a wider disturbed zone around the piles are found when increasing the water flow velocity from v_1 to v_2 (Fig. 11 c).

Streamlines are effective in reflecting water flow characteristics and understanding the mechanism of soil erosion (Kitsikoudis et al., 2017;

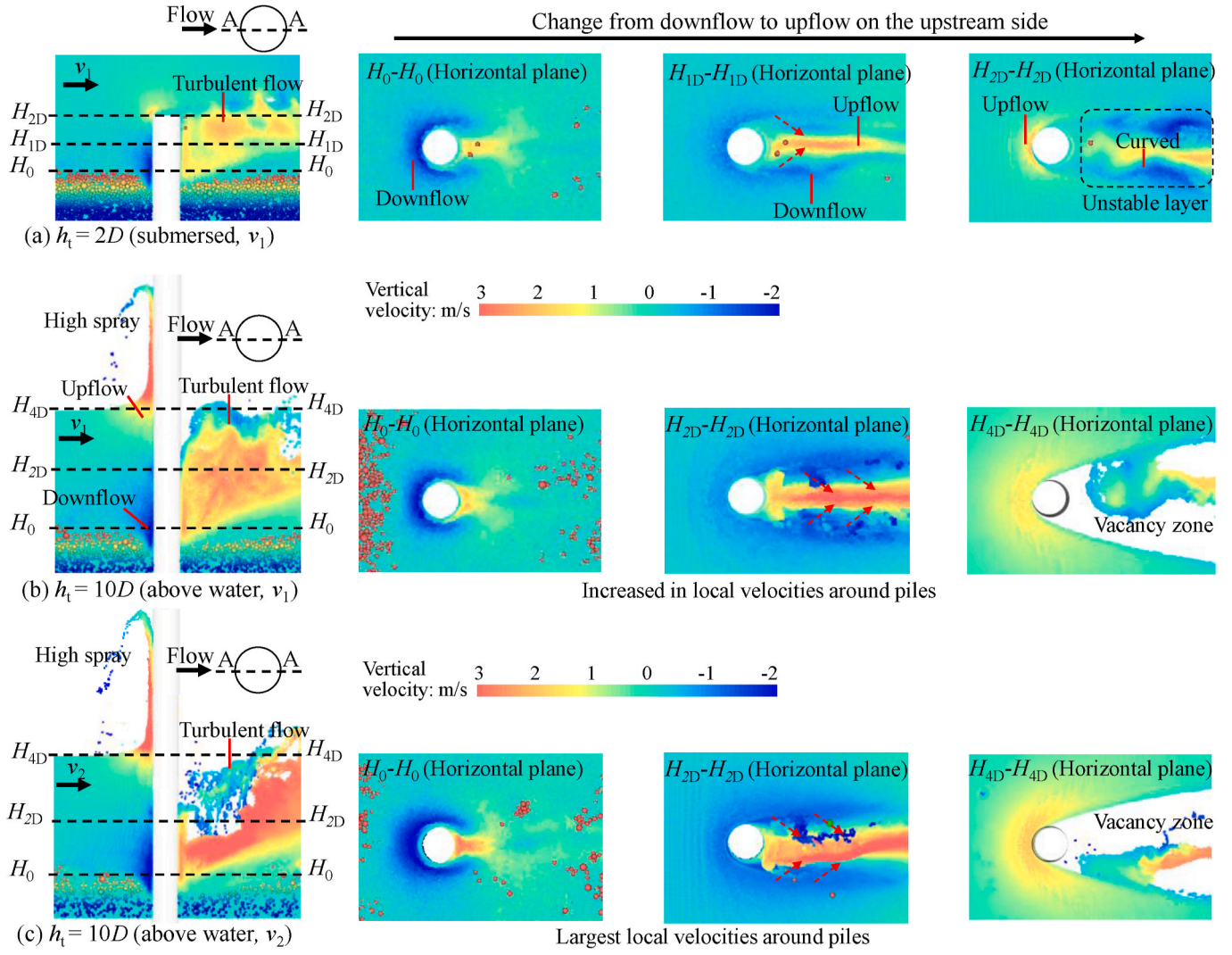

Fig. 11. Comparison of the water vertical flow velocity distributions around piles in different cases ($t = 5$s): (a) $h_t = 2D$ (submersed, v_1), (b) $h_t = 10D$ (above water, v_1), and (c) $h_t = 10D$ (above water, v_2).

Roulund et al., 2005). However, traditional CFD methods, which rely on fluid meshes, often struggle to accurately capture the complex directional changes of streamlines in highly turbulent regions, such as the local scour zone around piles (El-Emam et al., 2021; Zheng et al., 2024). Typical streamline distributions around piles under different scour lengths and flow velocities are illustrated in Fig. 12. Under a small scour length of $h_t = 1D$ (Fig. 12a), streamlines are straight and stable in the upper water layer but become noticeably curved in the layers passing the piles. In the water layer near the pile tops, a transition layer with curved and unstable streamlines is observed, which corresponds to the unstable turbulence indicated in Fig. 11a. Near the soil-water interface, streamlines turn downward on the upstream side and upward on the downstream side. The closer the streamlines are to the pile surfaces, the stronger the upflow on the downstream side. The upstream flow closest to the pile surface forms the 1_{st} layer of upflow on the downstream side, while upstream flows farther from the pile surfaces form the 2_{nd} and 3_{rd} layers of upflow with more gradual directional changes.

Comparing the streamlines in Fig. 12b and c with those in Fig. 12a, the effect of scour length on water flow becomes evident. As the scour length increases to $h_t = 10D$ (Fig. 12b), streamlines near the water surface exhibit a strong upward tendency on the upstream side, while those near the soil-water interface show a marked downward flow on the upstream side. The stronger squeezing of streamlines due to the longer pile length leads to stronger uplift flow on the downstream side. As the scour time increases from 0.5s to 5s in Fig. 12b and c, the zone of flow trajectories below the initial soil surface significantly expands around the piles due to the development of scour holes. Furthermore, Fig. 12c shows that the input flow velocity also significantly alters the streamlines around piles. Under the mean flow velocity of v_2, although the basic distributions of streamlines around piles are similar to those under the velocity of v_1, the zones of curved streamlines near the soil surface increase sharply. The swirling streamlines are prominently observable upstream, signifying the presence of robust vortices in these locations. Furthermore, the local streamlines at the scour hole positions reveal that the shape of streamlines around the scour hole closely resembles screw threads when subjected to high flow velocities. In summary, the streamlines in the coupled SPH-DEM simulations effectively model the local fluid flow trajectories and velocity distributions around piles in flowing waters.

The aforementioned vertical flowing water induces corresponding

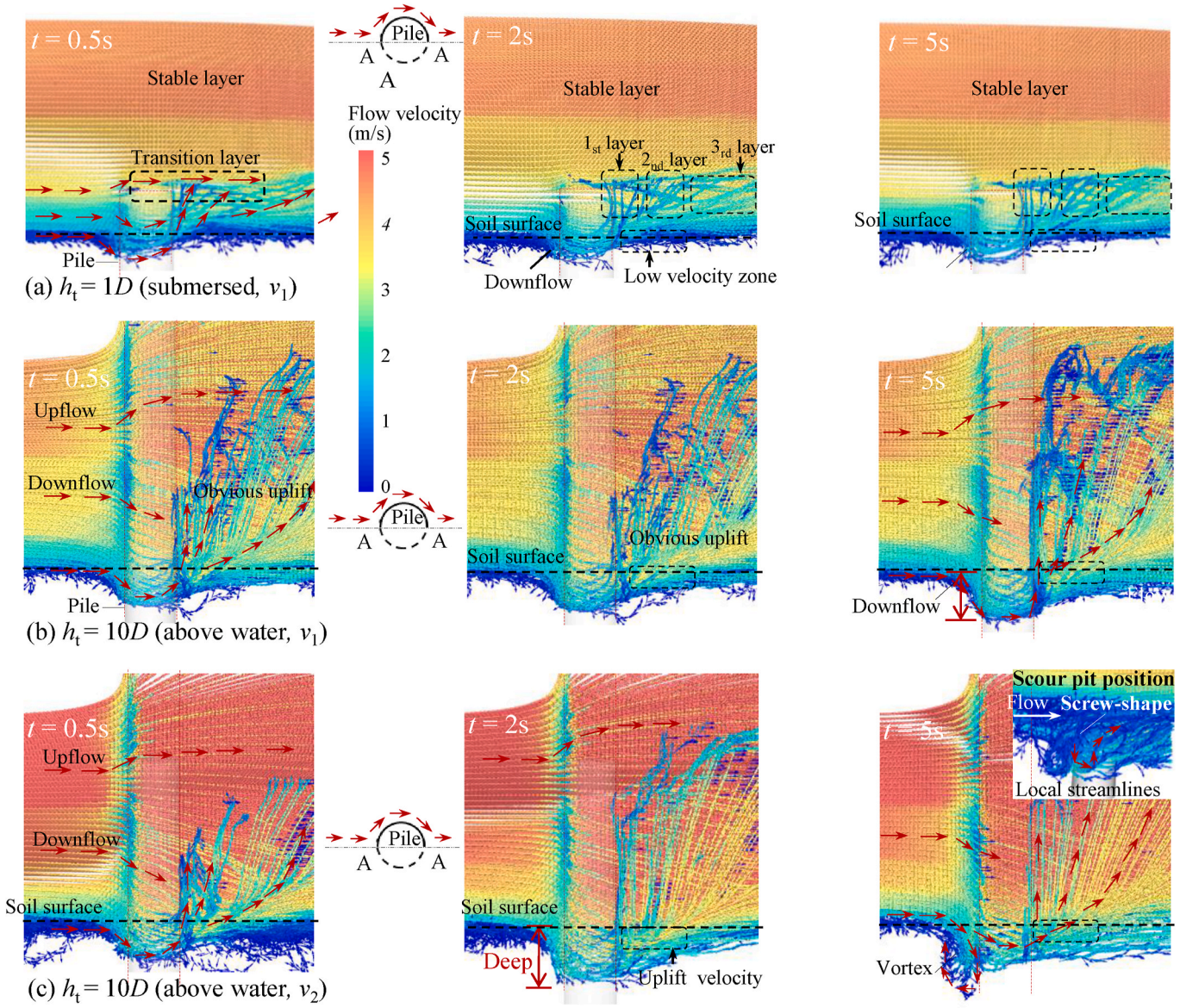

Fig. 12. Typical streamline distributions around piles in different cases (section A-A): (a) $h_t = 1D$ (submersed, v_1), (b) $h_t = 10D$ (above water, v_1), and (c) $h_t = 10D$ (above water, v_2).

vertical fluid forces on particles surrounding piles, further contributing to the soil erosion of granular soil (Liang et al., 2019; Liu et al., 2022; Zheng et al., 2024). Typical views of the vertical fluid forces on particles around piles are shown in Fig. 13. During the fast scour stage (t = 0.5s for example), the zone with high vertical fluid forces is widely distributed on the downstream side, closely correlating with the zone with high flow velocity in Fig. 8a. At this time, the reduction in the area of the water-crossing section due to pile obstruction leads to local turbulence on the downstream sides. As the process progresses into the progressive scour stage (t = 2s), the horizontal area with high vertical fluid forces decreases in Fig. 13, corresponding to the development of scour holes around piles. As it further develops into the stable flow stage (t = 5s), the zone with high vertical fluid forces is further decreased. This reduction in scour areas on the downstream sides is due to the gradual recovery of the water-crossing section area as the scour hole around piles develops. In the stable flow stage (t = 5s), the area with high vertical fluid forces is primarily distributed in a small zone behind the piles in the case of h_t = 1D (Fig. 13a), whereas it forms a circular shape surrounding the piles in the case of h_t = 10D (Fig. 13b and c). In fact, during the stable flow stage, the shape of the zone with high vertical fluid forces corresponds well to the local soil slope position of scour holes. As the flow velocity increases (Fig. 13 d), the zone with high vertical fluid forces expands into a gourd-shaped zone, which corresponds to the gourd-shaped scour hole that will be analyzed in detail in subsequent sections.

4.3. Analysis of local scour holes around piles

Studying local scour holes around piles is crucial for ensuring the stability and safety of hydraulic and coastal structures that rely on pile foundations (Wang et al., 2023, 2024b). In most previous experimental tests, measuring the detailed dimensions of equilibrium scour holes under flowing water conditions is challenging. Consequently, the dimensions of equilibrium scour holes around piles are typically measured after completing the tests and stopping the water flow. However, according to previous experiment studies (Du et al., 2023a; Yao et al., 2018), the actual scour holes observed during operation—when water flow is present—are usually deeper and larger than those observed after the flow has stopped. Therefore, a significant advantage of numerical simulations is their ability to present the scour holes under flowing water conditions.

To observe the soil erosion characteristics, the top view of moving particles around piles is shown in Fig. 14. In all cases, the intensity of particle sediment transport is strong at beginning and then gradually decreases, consistent with the mass-time curves in Fig. 10. At a scour time of t = 5s (into the stable flow stage), sediment transportation becomes very weak in all cases (see the images in the right column of Fig. 14). Compared to that in Fig. 14a, the intensity of particle moving in Fig. 14b is significantly stronger, demonstrating the important effect of scour length on soil erosion. In Fig. 14c, the intensity of particle moving is the greatest, corresponding to the largest scour hole in the simulations. After the balance of particle transportation and deposition around piles, equilibrium scour holes are formed. The equilibrium scour holes after stopping the flow (here defined as the stop-flow condition) are presented in Fig. 15a for analysis. In these simulations, after stopping the water flow at a scour time of t = 5s, the numerical cases continue to run for 10s to achieve a new water-soil equilibrium around the piles. Additionally, the actual equilibrium scour holes under flow conditions (t = 5s) are presented in Fig. 15b for further analysis. A comparison of the images in Figs. 15a and b shows that the difference in equilibrium scour holes between flow conditions and stop-flow conditions increases with the dimension of the initial scour holes. For example, in the cases of h_t = 10D with large and deep initial scour holes, there is a significant decrease in the slope and depth of scour holes after stopping water flow due to soil collapse around piles. This indicates that the difference in equilibrium scour holes between flow conditions and stop-flow conditions increases with scour length and flow velocity. Detailed information

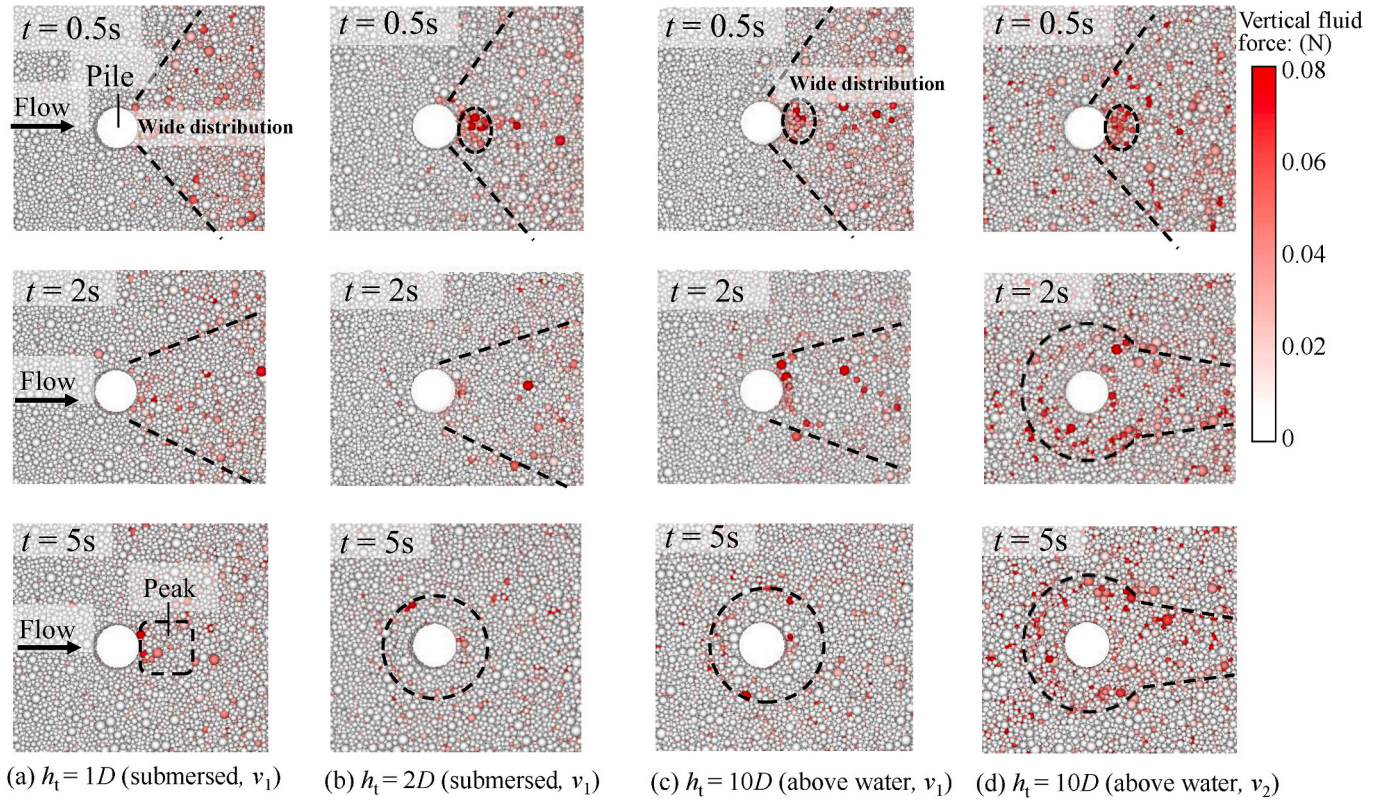

Fig. 13. Top view of the vertical fluid forces on particles around piles in different cases: (a) h_t = 1D (submersed, v_1), (b) h_t = 2D (submersed, v_1), (c) h_t = 10D (above water, v_1), and (d) h_t = 10D (above water, v_2).

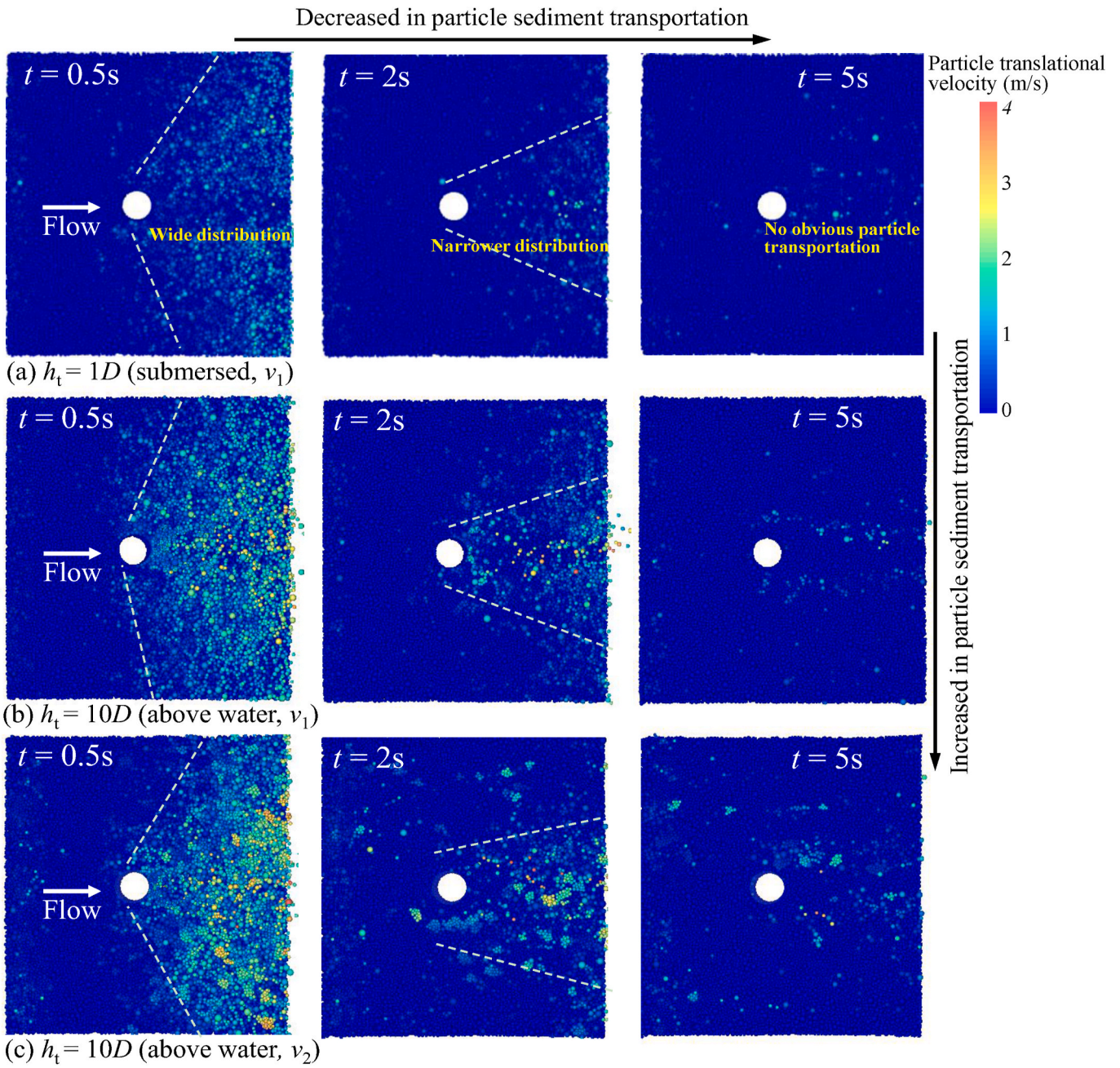

Fig. 14. Comparison of soil erosion distributions around piles in different cases: (a) $h_t = 1D$ (submersed, v_1), (b) $h_t = 10D$ (above water, v_1), and (c) $h_t = 10D$ (above water, v_2).

on the profiles of scour holes will be further analyzed in the following sections.

The outer boundary of scour holes is critical for determining the pile-affected zone in pile foundation designs (Chow and Herbich, 1978; Du et al., 2023a). While the depth and slope angle around piles change after the flow stop, the outer boundary of the scour holes remains essentially similar to that in flowing water conditions. The shape of outer boundaries of scour holes in different scenarios are summarized and analyzed in Fig. 16. The horizontal boundary of the scour hole in the case of short scour lengths is shown in Fig. 16a. Consistent with findings from previous experimental tests (Du et al., 2023b), the largest scour zone appears on the two sides of the piles due to significant streamlines squeezing at these locations. In this scenario, soil erosion on the downstream side of the piles is weak, and some of the transported particles are deposited behind the piles. As shown in Fig. 16b, with an increase in the scour length of piles, the shape of the outer boundary of the scour holes gradually transitions to an approximately circular shape, consistent with the previous studies (Jia et al., 2023; Yao et al., 2018). This evolution in shape can be explained by the increased local flow velocities and the formation of vortex flow on the downstream side. In Fig. 16c, with a further increase in flow velocity, the squeezing of streamlines intensifies, resulting in a high upflow velocity on the downstream side of the piles, which leads to the extension of the scour trail.

Investigating the vertical profiles of scour holes around piles is crucial for understanding detailed soil erosion dynamics. Fig. 17 presents typical vertical soil profiles around piles to further analyze the characteristics of scour holes. These soil profiles clearly indicate that the depth and slope angles of the holes around piles under the flow conditions are significantly larger than those under stop-flow conditions. The

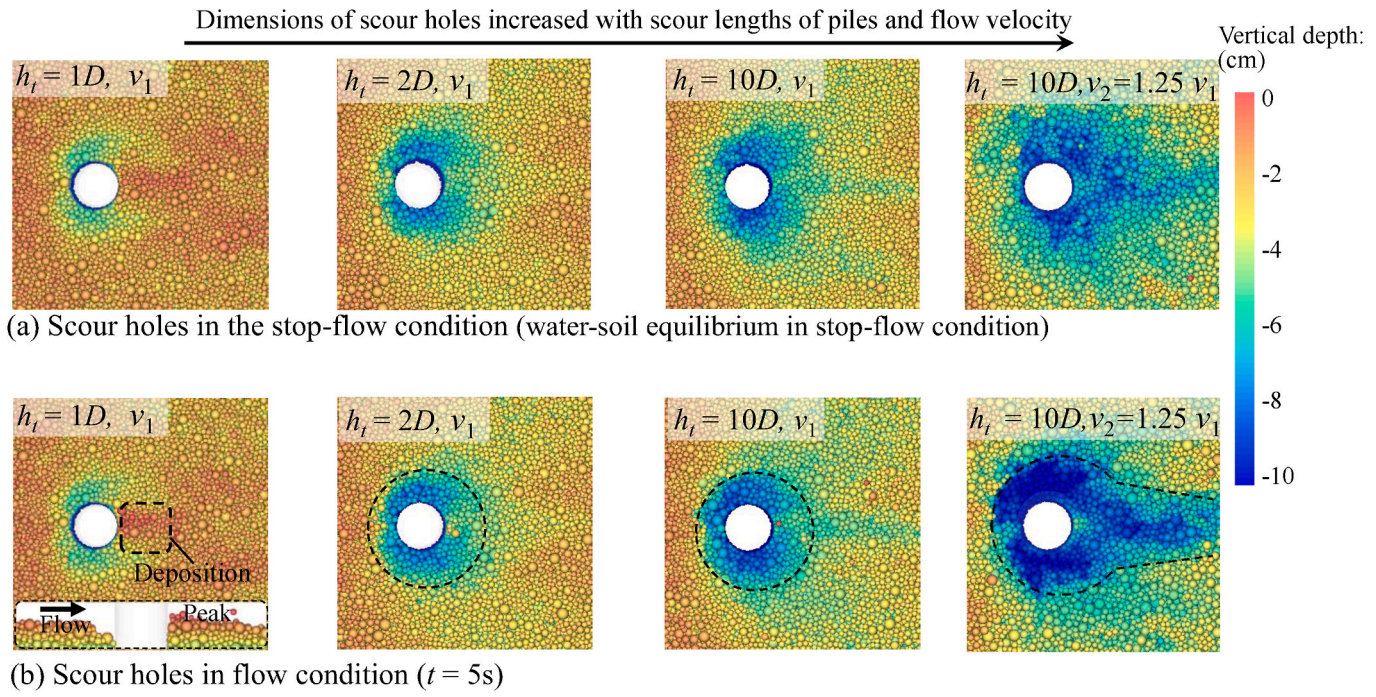

Fig. 15. Comparison of the top view results of scour holes around piles: (a) Scour holes in the stop-flow condition (water-soil equilibrium in stop-flow condition), (b) Scour holes in flow condition (t = 5s).

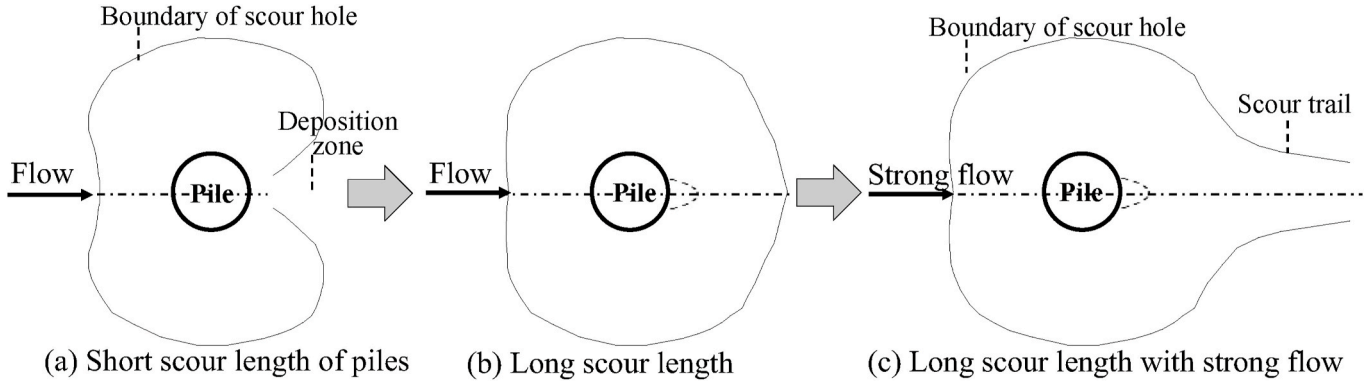

Fig. 16. Comparison of the horizontal boundary of scour hole around piles in different cases: (a) Short scour length of piles, (b) Long scour length, and (c) Long scour length with strong flow.

soil section along the flow direction (section A-A) in Fig. 17a shows that the width of the scour holes on the upstream side is about 2.0–2.5 times the pile diameter (D), while the soil surface deformations on the downstream side vary greatly. Under a low scour length of $h_t = 1D$, an upslope zone, rather than holes, is observed on the downstream side, induced by sediment deposition from upstream particles as noted in previous studies (Du and Liang, 2019; Du et al., 2023b). Due to the flow motion over the sedimentary zone (upslope), the vertical fluid force in this zone is much larger than in other areas, explaining the existence of a particularly high fluid force zone shown in Fig. 13a. Under a long scour length of $h_t = 10D$, the scour holes extend downstream with relatively long scour zones. In this situation, the slope angle at the outer boundary of the holes is steep, accounting for the intense upflow and thus large vertical fluid force on the slopes of holes, as seen in Fig. 13b–d. Additionally, the soil section perpendicular to the flow direction (section B-B) is shown in Fig. 17b. The soil sections in Fig. 17b indicate that the maximum depth of scour holes in the simulations is significantly greater than 1D, while the horizontal pile-affected width is about 2.5 times the pile diameter (D). These findings underscore the significant impact of scour length and flow velocity on the morphology of scour holes around piles.

Further statistical analysis of local scour depth at the two sides of piles in SPH-DEM simulations is presented in Table 2 and Fig. 18, demonstrating the significant impact of scour length and flow velocity on local scour depth. As flow velocity or scour length increases, the standard deviation of local scour depth at both sides of the pile rises obviously, indicating that the deviation in predicting local scour depth increases with flow velocity and scour length when using the SPH-DEM method. This increase in the deviation should be attributed to the heightened randomness and intensity of turbulence resulting from the increased flow velocity and scour length. Additionally, the statistical analysis of the effect of scour length presented in Fig. 18 preliminarily reveals that the sensitivity of scour depth to scour length is more pronounced when the scour length does not exceed 2D.

After conducting individual analyses of streamline distributions, fluid forces on soil particles, distributions of moving particles, and dimensions of scour holes, this section presents a comprehensive transition analysis. Fig. 19 presents comprehensive data around the piles,

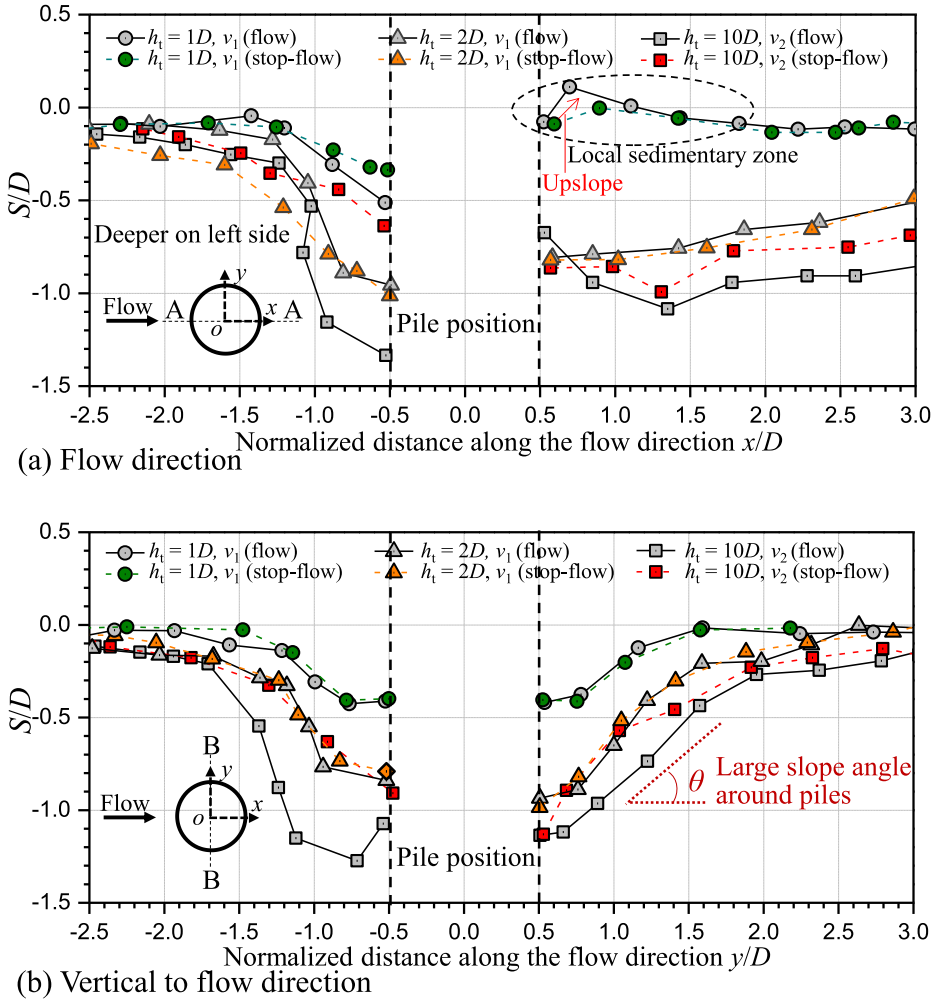

Fig. 17. Comparison of the vertical soil profiles around piles in the flow and the stop-flow conditions: (a) Flow direction (section A-A), and (b) Vertical to flow direction (section B-B).

Table 2
Statistical analysis of local scour depth at pile sides in SPH-DEM simulations.

Cases		Local scour depth at pile sides S/D		Arithmetic mean	Standard Deviation
		Left side	Right side		
Flow condition	$h_t = 1D$, v_1	−0.42	−0.43	−0.425	0.005
	$h_t = 2D$, v_1	−0.95	−0.84	−0.895	0.055
	$h_t = 10D$, v_1	−1.23	−1.10	−1.165	0.065
	$h_t = 10D$, v_2	−1.15	−1.29	−1.22	0.07
Stop-flow condition	$h_t = 1D$, v_1	−0.4	−0.41	−0.405	0.005
	$h_t = 2D$, v_1	−0.93	−0.8	−0.865	0.065
	$h_t = 10D$, v_1	−1.01	−0.87	−0.94	0.07
	$h_t = 10D$, v_2	−1.13	−0.91	−1.02	0.11

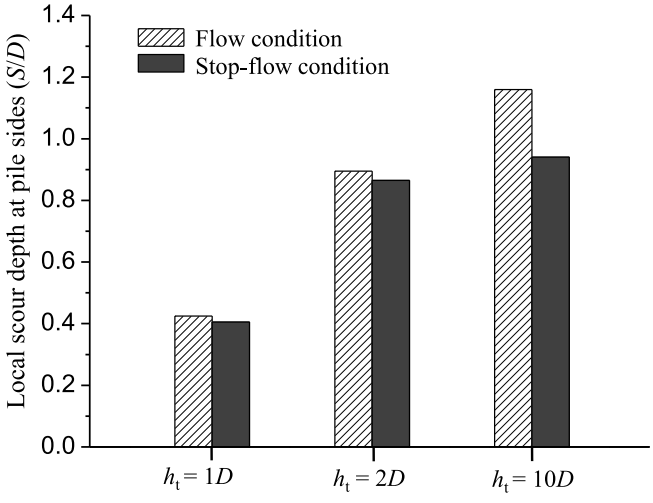

Fig. 18. Statistical analysis of scour length effect on the local scour depths at pile sides.

including the distributions of fast-moving particles (only those with velocities exceeding 0.5 m/s), streamlines of the local flow field, and semitransparent vertical sections of the scour holes. In these images, blue streamlines indicate downward flow, while red streamlines represent upward flow. The fluid force acting on each particle is represented by the color of the particle, while the relative velocity is illustrated by an arrow. When the water flow encounters the mild obstruction caused by short piles, as shown in Fig. 19a, the cross-

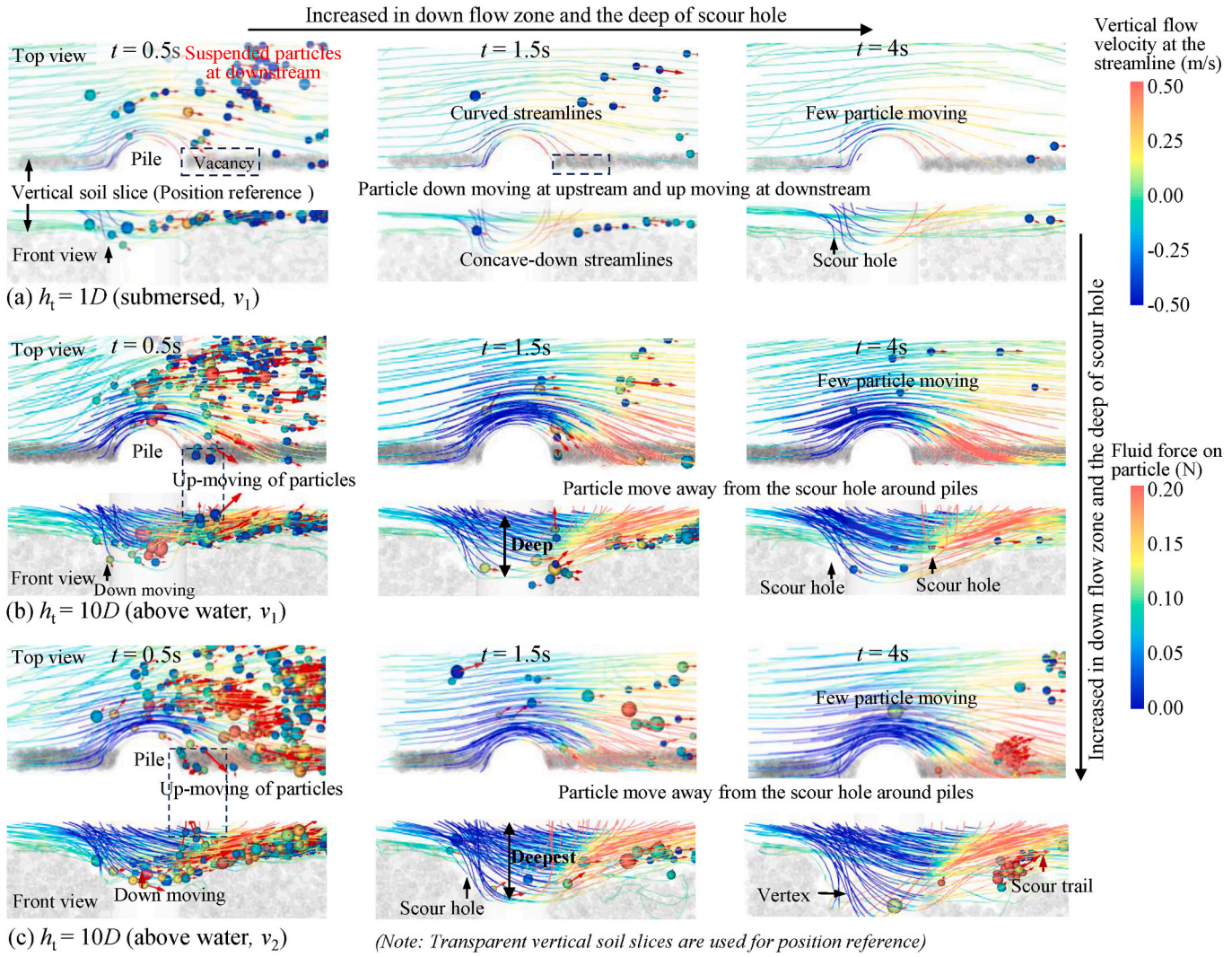

Fig. 19. A comprehensive comparison of the particle movement, flow field, and soil erosion around piles: (a) $h_t = 1D$ (submersed, v_1), (b) $h_t = 10D$ (above water, v_1), and (c) $h_t = 10D$ (above water, v_2).

sectional area of the water flow is slightly reduced, resulting in an increase in flow intensity around the pile, indicated by the local denser streamlines. The increase in local flow intensity causes noticeable particle movement on the pile side with a significant number of suspended particles at the downstream side, in the initial scour stage ($t = 0.5$ s). As scour progresses ($t = 1.5$ s and 4 s), the particle movement near the piles leads to the development of concave-down streamlines (also see Figs. 11 and 12), causing a slight downward flow and particle movement at the upstream side of piles. Interestingly, the obstruction caused by the short piles creates a weak flow zone behind the pile, which could serve as a sedimentary zone for moving particles (also see Figs. 13 and 15).

As the scour length of the piles significantly increases, as shown in Fig. 19b, the cross-sectional area of the water flow decreases sharply, resulting in denser local streamlines around the pile. This change corresponds to a much stronger fluid force, faster particle motion, and distinctly concave-down streamlines. The enhanced local flow intensity allows water, along with the transported particles, to flow fast behind the pile, facilitating particle movement in that zone. As scour time increases (t = 1.5 s and 4s in Fig. 19b), the moving particles primarily originate from the scour hole surrounding the piles. This leads to a gradual broadening of the scour hole in both the upstream and downstream directions, with increasing depth. As the flow velocity further increases, as shown in Fig. 19c, the streamlines become densest surrounding the pile, corresponding to the strongest downward motion of particles at the upstream side and upward motion at the downstream side. As scour time progresses ($t = 1.5$ s and 4 s in Fig. 19c), the increased flow intensity results in the highest particle velocity (kinetic energy) and the strongest upward flow behind the pile (also see Figs. 11 and 12). This leads to the formation of the deepest scour hole with a scour trail behind the pile.

A comprehensive series of macro- and micro-scale analyses of water-pile-soil interactions have illustrated the fundamental patterns of scour behavior around piles, as depicted in Fig. 20. Under short scour length conditions (Fig. 20a), the scour hole primarily forms on the upstream side of the piles, with a localized particle sedimentation zone behind the piles, consistent with the previous experimental studies (Du and Liang, 2019; Liang et al., 2016). In contrast, under long scour length conditions (Fig. 20b), scour holes develop behind the piles, accompanied by a pronounced backflow vortex on the upstream side, consistent with the previous studies (Jia et al., 2023; Liang et al., 2016). Here, the scour hole takes on a nearly circular shape with deep scour zones. Under conditions of long scour length combined with strong flow (Fig. 20c), scour holes evolve further around the piles, with intense backflow vortex on the upstream side and vortex flow behind the piles. In this scenario, the scour hole deepens, displaying a distinct scour trail on the downstream side. In summary, the scour length of piles in flowing water significantly influences the scour behavior around piles. Thus, neglecting the effects of scour length and flow velocity can lead to misjudgments regarding the

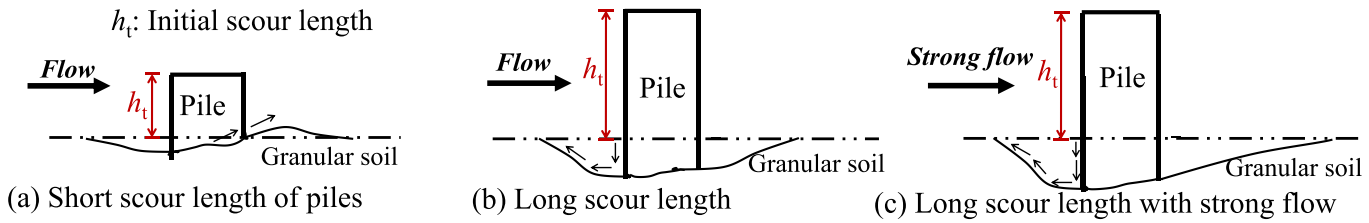

Fig. 20. Schematic diagram of patterns of scour behaviors around circular piles under different conditions: (a) Short scour length of pile, (b) Long scour length, and (c) Long scour length with strong flow.

scour zone and scour intensity, thereby posing potential risks to the safety of pile foundations in flowing water.

5. Conclusions

This study addresses an obvious gap in local scour mechanics around circular piles in granular soil through the novel implementation of a coupled SPH-DEM approach, which integrates fluid-particle interactions from macro to microscales. The main findings of this investigation are outlined below.

(1) The development of turbulent regions and soil erosion around piles can be effectively captured in the coupled SPH-DEM simulations. Overall, both scour length and flow velocity are proven to be important factors that affect the intensity of soil erosion. As scour time increases, lateral flow velocity and the horizontal turbulence zone decrease significantly around the water-soil interface but change less in the water layer further from the interface. Additionally, the evolution curves of soil scour loss are useful in dividing the scour process into 3 stages including the fast scour stage, progressive scour stage, and stable flow stage.

(2) The effects of flow velocity and scour length on flow characteristics around piles have been discovered. On the whole, the degree of water deformation and turbulence intensity are found to increase with flow velocities in the SPH-DEM simulations. For piles with short scour lengths under immersed conditions, an oscillating flow layer is observed on pile tops, while the main turbulence zone with large deformation emerges on the downstream side of piles. For piles with long scour lengths above water, strong turbulent flow is observed on the downstream side while significant spray with large deformation is found on the upstream side.

(3) Relationships between local flow direction, vortexes, and soil erosion can be identified by analyzing streamlines and fluid forces on particles in SPH-DEM simulations. The streamlines have been proven to be effective in reflecting the local flow directions and turbulence zones, while the up-curved degree of downstream streamlines has been discovered to be negatively related to distance to the lateral pile surfaces. Besides, the local vortexes and soil erosion are found to be heavily increased with scour lengths and flow velocities. In addition, vertical fluid forces on particles are found to be related to both turbulence viscosity and the local slope topography of scour holes.

(4) Scour patterns around circular piles are derived from analyzing particle behaviors and the development of scour holes. The equilibrium scour depth for a long pile with a scour length of 2D is approximately twice that of a pile with a smaller scour length of 1D, highlighting the significant impact of pile length on scour depths around piles. Besides, under short scour lengths, a deposition zone emerges on the downstream side, while the scour holes are developed on the downstream side under long scour lengths. Finally, three definitive scour patterns influenced by scour length and flow velocity have been concluded based on the above macro-to-micro scour behaviors.

In summary, this study bridges a noteworthy research gap by pioneering the use of coupled SPH-DEM simulations to investigate local scour around circular piles in granular soil under steady flow conditions. By capturing particle-scale interactions and turbulent flow dynamics, the SPH-DEM approach provides novel insights into scour mechanisms, offering a significant advancement over traditional continuum-based methods. The findings contribute to a deeper understanding of scour progression and provide a reference for the development of more effective scour protection strategies in riverine and marine environments.

CRediT authorship contribution statement

Yu Peng: Writing – original draft, Validation, Software, Methodology, Investigation, Formal analysis, Data curation, Conceptualization. **Zhen-Yu Yin:** Writing – review & editing, Resources, Project administration, Methodology, Funding acquisition, Conceptualization.

Data availability statement

All data that support the findings of this study are available from the corresponding author upon reasonable request.

Declaration of competing interest

The authors declare that they have no known competing financial interests or personal relationships that could have appeared to influence the work reported in this paper.

Acknowledgments

This work was supported by the general research fund of the Research Grants Council (RGC) of the Hong Kong Special Administrative Region Government (HKSARG) of China (grant No. 15232224, 15229223).

References

Abou-Seida, M., Elsaeed, G., Mostafa, T., Elzahry, E., 2009. Experimental investigation of abutment scour in sandy soil. J. Appl. Sci. Res. 5 (1), 57–65.
Ahmad, N., Bihs, H., Kamath, A., Arntsen, Ø.A., 2016. 3D Numerical modelling of pile scour with free surface profile under waves and current using the level set method in model REEF3D. Proceedings of Scour and Erosion—Proceedings of the 8th International Conference on Scour and Erosion. Mathematical Institute Oxford, UK, pp. 69–76.
Ahmadianfar, I., Jamei, M., Karbasi, M., Sharafati, A., Gharabaghi, B.J.E.w.C., 2022. A novel boosting ensemble committee-based model for local scour depth around non-uniformly spaced pile groups, 38 (4), 3439–3461.
Amini Baghbadorani, D., Beheshti, A.-A., Ataie-Ashtiani, B., 2017. Scour hole depth prediction around pile groups: review, comparison of existing methods, and proposition of a new approach. Nat. Hazards 88, 977–1001.
Arroyo, M., Butlanska, J., Gens, A., Calvetti, F., Jamiolkowski, M., 2011. Cone penetration tests in a virtual calibration chamber. Geotechnique 61 (6), 525–531.
Bagheri, M., Mohammadi, M., Riazi, M., 2024. A review of smoothed particle hydrodynamics. J Computational Particle Mechanics 11 (3), 1163–1219.
Bateni, S., Jeng, D.-S.J.O.E., 2007. Estimation of pile group scour using adaptive neuro-fuzzy approach, 34 (8–9), 1344–1354.
Bernhardt, M.L., Biscontin, G., 2016. Experimental validation study of 3D direct simple shear DEM simulations. Soils Found. 56 (3), 336–347.

Beven, K., Germann, P., 2013. Macropores and water flow in soils revisited. Water Resour. Res. 49 (6), 3071–3092.
Chang, W.-Y., Lai, J.-S., Yen, C.-L., 2004. Evolution of scour depth at circular bridge piers. J. Hydraul. Eng. 130 (9), 905–913.
Chaussonnet, G., Braun, S., Wieth, L., Koch, R., Bauer, H.-J., 2015. Influence of Particle Disorder and Smoothing Length on SPH Operator Accuracy. 10th International SPHERIC Workshop, p. 8.
Chen, X., Bai, B., 2015. Experimental investigation and modeling of particulate transportation and deposition in vertical and horizontal flows. Hydrogeol. J. 23 (2), 365.
Chen, Y., Deng, A., Wang, A., Sun, H., 2018. Performance of screw–shaft pile in sand: model test and DEM simulation. Comput. Geotech. 104, 118–130.
Chiew, Y.-M., Melville, B.W., 1987. Local scour around bridge piers. J. Hydraul. Res. 25 (1), 15–26.
Chiew, Y.M., 1990. Mechanics of local scour around submarine pipelines. J. Hydraul. Eng. 116 (4), 515–529.
Chow, W.-Y., Herbich, J.B., 1978. Scour Around a Group of Piles, Offshore Technology Conference. OTC. OTC-3308-MS.
Cil, M.B., Sohn, C., Buscarnera, G., 2020. DEM modeling of grain size effect in brittle granular soils. J. Eng. Mech. 146 (3), 04019138.
Cleary, P.W., 1998. Modelling confined multi-material heat and mass flows using SPH. Appl. Math. Model. 22 (12), 981–993.
Coetzee, C., Els, D., 2009. Calibration of granular material parameters for DEM modelling and numerical verification by blade–granular material interaction. J. Terramechanics 46 (1), 15–26.
Colagrossi, A., Landrini, M., 2003. Numerical simulation of interfacial flows by smoothed particle hydrodynamics. J. Comput. Phys. 191 (2), 448–475.
Cundall, P., Strack, O., 1979. A discrete Element Method for granular assemblies. Geotechnique 29 (1), 47–65.
Das, S., Das, R., Mazumdar, A., Sciences, E., 2014. Variations of clear water scour geometry at piers of different effective widths. Turkish Journal of Engineering 38 (1), 97–111.
Dey, S., 2014. Fluvial Hydrodynamics. Springer, Berlin Heidelberg.
Du, S., Liang, B.J.W., 2019. Comparisons of local scouring for submerged square and circular cross-section piles in steady currents. Water 11 (9), 1820.
Du, S., Wang, C., Zhang, Z., Wu, G., Liang, B., 2023a. Experimental study of local scour around circularcrossing and square-crossing piles in waves and current. J. Mar. Environ. Eng. 11 (1).
Du, S., Wu, G., Liang, B., Zhu, D.Z., Wang, R., 2023b. Experimental study of submergence ratio on local scour around a square pile in steady flow. J. Ocean Univ. China 22 (5), 1277–1288.
Dutta, D., Afzal, M.S., Alhaddad, S., 2023. 3D CFD study of scour in combined wave–current flows around rectangular piles with varying aspect ratios. Water 15 (8), 1541.
El-Emam, M.A., Zhou, L., Shi, W., Han, C., Bai, L., Agarwal, R., 2021. Theories and applications of CFD–DEM coupling approach for granular flow: a review. Arch. Comput. Methods Eng. 28 (7), 4979–5020.
Ergun, S.J.C.e.p., 1952. Fluid flow through packed columns. Chemische Technik. Verfahrenstechnik. 48 (2), 89.
Fahmi, A.M., Ghaderi, S., Azizkandi, A.S., 2024. Micro–macro assessment of the pile bearing capacity interaction with single and double voids in different soil densities using the discrete-element method. Int. J. GeoMech. 24 (10), 04024220.
Falagush, O., McDowell, G., Yu, H.-S., 2015. Discrete element modeling of cone penetration tests incorporating particle shape and crushing. Int. J. GeoMech. 15 (6), 04015003.
Feng, H., Yin, Z.-Y., Peng, M., 2024. Macro-element modelling for lateral response of monopiles with local scour hole via hyperbolic hardening relation. Appl. Ocean Res. 153, 104233.
Gao, D., Pan, X., Liang, B., Yang, B., Wu, G., Wang, Z., 2024. A review and design principle of fixed-bottom foundation scour protection schemes for offshore wind energy. J. Mar. Sci. Eng. 12 (4), 660.
Gezgin, A.T., Soltanbeigi, B., Cinicioglu, O., 2020. Discrete-element modelling of pile penetration to reveal influence of soil characteristics. Proceedings of the Institution of Civil Engineers-Geotechnical Engineering 175 (4), 365–382.
Guan, D., Hsieh, S.-C., Chiew, Y.-M., Low, Y.M., 2019. Experimental study of scour around a forced vibrating pipeline in quiescent water. Coast. Eng. 143, 1–11.
Guo, Y., Curtis, J.S., 2015. Discrete element method simulations for complex granular flows. Annu. Rev. Fluid Mech. 47 (1), 21–46.
He, Y., Bayly, A.E., Hassanpour, A., Muller, F., Wu, K., Yang, D., 2018. A GPU-based coupled SPH-DEM method for particle-fluid flow with free surfaces. Powder Technol. 338, 548–562.
Heibaum, M., 2004. Geotechnical filters–The important link in scour protection. Proc. 2nd International Conference on Scour and Erosion.
Hu, D., Tang, W., Sun, L., Li, F., Ji, X., Duan, Z., 2019. Numerical simulation of local scour around two pipelines in tandem using CFD–DEM method. Appl. Ocean Res. 93, 101968.
Jensen, R.P., Edil, T.B., Bosscher, P.J., Plesha, M.E., Kahla, N.B., 2001a. Effect of particle shape on interface behavior of DEM-simulated granular materials. Int. J. GeoMech. 1 (1), 1–19.
Jensen, R.P., Plesha, M.E., Edil, T.B., Bosscher, P.J., Kahla, N.B., 2001b. DEM simulation of particle damage in granular media—structure interfaces. Int. J. GeoMech. 1 (1), 21–39.
Jia, X., Zhang, H., Wang, C., Liang, F., Chen, X., 2023. Influence on the lateral response of offshore pile foundations of an asymmetric heart-shaped scour hole. Appl. Ocean Res. 133, 103485.
Jiang, J., Yu, Y., Gong, J., Fu, C., 2024. Analytical method for lateral capacity of pile foundations under vertical loads considering asymmetric scour hole in sand. Ocean Eng. 293, 116654.
Jo, Y.B., Park, S.-H., Yoo, H.S., Kim, E.S., 2022. GPU-Based SPH-DEM method to examine the three-phase hydrodynamic interactions between multiphase flow and solid particles. Int. J. Multiphas. Flow 153.
Kitsikoudis, V., Kirca, V.O., Yagci, O., Celik, M.F., 2017. Clear-water scour and flow field alteration around an inclined pile. Coast. Eng. 129, 59–73.
Li, Y., Xu, Y., Thornton, C., 2005. A comparison of discrete element simulations and experiments for 'sandpiles' composed of spherical particles. Powder Technol. 160 (3), 219–228.
Liang, B., Du, S., Pan, X., Zhang, L., 2019. Local scour for vertical piles in steady currents: review of mechanisms, influencing factors and empirical equations. J. Mar. Sci. Eng. 8 (1), 4.
Liang, F.-y., Wang, C., Huang, M.-s., Li, J., 2016. Scale effects on local scour configurations around caisson foundation and dynamic evolution. China J. Highw. Transp. 29 (9), 59–67.
Lin, J., Naceur, H., Coutellier, D., Laksimi, A., 2015. Geometrically nonlinear analysis of two-dimensional structures using an improved smoothed particle hydrodynamics method. Eng. Comput. 32 (3), 779–805.
Liu, Q., Wang, Z., Zhang, N., Zhao, H., Liu, L., Huang, K., Chen, X., 2022. Local scour mechanism of offshore wind power pile foundation based on CFD-DEM. J. Mar. Sci. Eng. 10 (11), 1724.
Ma, H., Li, B., Zhang, S., 2024. Scour mechanism around a pipeline under different current-wave conditions using the CFD-DEM coupling model. Comput. Geotech. 170, 106304.
Macaro, G., Utili, S., Martin, C., 2015. DEM analyses of pipe–soil interaction for offshore pipelines on sand. In: Soga, K., Krishna Kumar, K., Biscontin, G. (Eds.), Geomechanics from Micro to Macro. Taylor and Francis, London.
Manenti, S., Sibilla, S., Gallati, M., Agate, G., Guandalini, R., 2012. SPH simulation of sediment flushing induced by a rapid water flow. J. Hydraul. Eng. 138 (3), 272–284.
Mao, W., Wang, Y., Yang, P., Huang, Y., Zheng, H., 2023. Dynamics of granular debris flows against slit dams based on the CFD–DEM method: effect of grain size distribution and ambient environments. Acta Geotechnica 18 (11), 5811–5838.
Melville, B., Sutherland, A., 1988. Design method for local scour at bridge piers. J. Hydraul. Eng. 114 (10), 1210–1226.
Monaghan, J.J., 1989. On the problem of penetration in particle methods. J. Comput. Phys. 82 (1), 1–15.
Monaghan, J.J., 1992. Smoothed particle hydrodynamics. Annu. Rev. Astron. Astrophys. 30, 543–574.
Monaghan, J.J., 2000. SPH without a tensile instability. J. Comput. Phys. 159 (2), 290–311.
Monaghan, J.J., 2012. Smoothed particle hydrodynamics and its diverse applications. Annu. Rev. Fluid Mech. 44 (1), 323–346.
Najafzadeh, M., Azamathulla, H.M., 2015. Neuro-fuzzy GMDH to predict the scour pile groups due to waves. J. Comput. Civ. Eng. 29 (5), 04014068.
Najafzadeh, M., Bento, A.M., Basirian, S., Fazeres-Ferradosa, T., 2025. Dynamic damage functions for scour protection at monopile foundations: application of ensemble machine learning models. Ocean Eng. 323, 120590.
Najafzadeh, M., Sheikhpour, R., 2024. Local scour depth at piles group exposed to regular waves: on the assessment of expressions based on classification concepts and evolutionary algorithms. Results in Engineering 21, 101810.
Ng, K., Ng, Y., Sheu, T., Alexiadis, A., 2020. Assessment of Smoothed Particle Hydrodynamics (SPH) models for predicting wall heat transfer rate at complex boundary. Eng. Anal. Bound. Elem. 111, 195–205.
Ozgoren, M., 2006. Flow structure in the downstream of square and circular cylinders. Flow Meas. Instrum. 17 (4), 225–235.
Peng, Y., Liu, H., Li, C., Ding, X., Deng, X., Wang, C., 2021. The detailed particle breakage around the pile in coral sand. Acta Geotechnica 16 (6), 1971–1981.
Peng, Y., Yin, Z.-Y., 2023. Micromechanical analysis of suction pile-granular soil interaction under inclined pulling load of mooring line: mooring depth effect. Mar. Struct. 92, 103499.
Peng, Y., Yin, Z.-Y., Ding, X., 2022. Analysis of particle corner-breakage effect on pile penetration in coral sand: model tests and DEM simulations. Can. Geotech. J.
Petersen, T.U., Mutlu Sumer, B., Fredsøe, J., Raaijmakers, T.C., Schouten, J.-J., 2015. Edge scour at scour protections around piles in the marine environment — laboratory and field investigation. Coast. Eng. 106, 42–72.
Potapov, A.V., Hunt, M.L., Campbell, C.S., 2001. Liquid–solid flows using smoothed particle hydrodynamics and the discrete element method. Powder Technol. 116 (2–3), 204–213.
Quezada, M., Tamburrino, A., Niño, Y., 2018. Numerical simulation of scour around circular piles due to unsteady currents and oscillatory flows. Engineering Applications of Computational Fluid Mechanics 12 (1), 354–374.
Robinson, M., Ramaioli, M., Luding, S., 2014. Fluid–particle flow simulations using two-way-coupled mesoscale SPH–DEM and validation. Int. J. Multiphas. Flow 59, 121–134.
Roulund, A., Sumer, B.M., Fredsoe, J., Michelsen, J., 2002. 3-D numerical modeling of flow and scour around a pile. Proc. First Intl Conf. on Scour of Foundations 17–20.
Roulund, A., Sumer, B.M., Fredsøe, J., Michelsen, J., 2005. Numerical and experimental investigation of flow and scour around a circular pile. J. Fluid Mech. 534, 351–401.
Russell, T.F., Wheeler, M.F., 1983. Finite Element and Finite Difference Methods for Continuous Flows in Porous Media, the Mathematics of Reservoir Simulation. SIAM, pp. 35–106.
Sizkow, S.F., El Shamy, U., 2022. SPH-DEM modeling of the seismic response of shallow foundations resting on liquefiable sand. Soil Dynam. Earthq. Eng. 156, 107210.

Soroush, A., Shourijeh, P.T., Fouladi, S.R., 2019. The effects of soil erosion characteristics on critical filter design in embankment dams. Geotech. Test. J. 42 (3), 789–816.
Su, Z., Wang, S., Li, D., Sheng, J., Wu, W., 2024. SPH–DEM modeling overtopping failure of earthfill dams. Acta Geotechnica 19, 953–970.
Sumer, B., Christiansen, N., Fredsoe, J., 1992. Time scale of scour around a vertical pile. ISOPE International Ocean and Polar Engineering Conference. ISOPE. ISOPE-I-92-259.
Sumer, B.M., Whitehouse, R.J., Tørum, A., 2001. Scour around coastal structures: a summary of recent research. Coast. Eng. 44 (2), 153–190.
Tafarojnoruz, A., Lauria, A., 2020. Large eddy simulation of the turbulent flow field around a submerged pile within a scour hole under current condition. Coast. Eng. J. 62 (4), 489–503.
Tan, S.M., Lim, S.-Y., Wei, M., Cheng, N.-S., 2020. Application of particle densimetric Froude number for evaluating the maximum culvert scour depth. J. Irrigat. Drain. Eng. 146 (8), 04020020.
Tavarez, F.A., Plesha, M.E., 2007. Discrete element method for modelling solid and particulate materials. Int. J. Numer. Methods Eng. 70 (4), 379–404.
Ting, J.M., Corkum, B.T., Kauffman, C.R., Greco, C., 1989. Discrete numerical model for soil mechanics. Journal of Geotechnical Engineering 115 (3), 379–398.
Violeau, D., Issa, R., 2007. Numerical modelling of complex turbulent free-surface flows with the SPH method: an overview. Int. J. Numer. Methods Fluid. 53 (2), 277–304.
Wang, C., Wang, Y., Peng, C., Meng, X., 2016. Smoothed particle hydrodynamics simulation of water-soil mixture flows. J. Hydraul. Eng. 142 (10), 04016032.
Wang, L., Wu, W., El Naggar, M.H., Zhang, Y., Liu, X., Sun, J., 2024a. Scoured failure wedge model for analysis of scoured pile-soil interaction in sand. Comput. Geotech. 166, 105981.
Wang, S.-T., Reese, L.C., 1988. Development of a laboratory test to identify the scour potential of soils at piles supporting offshore structures. US Army Engineer Waterways Experiment Station, Geotechnical Laboratory.
Wang, S.-Y., Qi, W.-G., Gao, F.-P., Li, B., He, B., 2024b. Time development of clear-water scour around a pile foundation: phenomenological theory of turbulence-based approach. Coast. Eng. 190, 104511.
Wang, T., Zhang, F., Furtney, J., Damjanac, B., 2022a. A review of methods, applications and limitations for incorporating fluid flow in the discrete element method. J. Rock Mech. Geotech. Eng. 14 (3), 1005–1024.
Wang, Z., Zhou, H., Franza, A., Liu, H., 2022b. Numerical evaluation of scour effects on lateral behavior of pile groups in clay. Comput. Geotech. 150, 104913.
Wang, Z., Zhou, H., Sheil, B., Liu, H., Wang, C., 2023. Numerical investigation of the lateral response of pile groups in sand under local scour conditions. Comput. Geotech. 159, 105435.
Wensrich, C., Katterfeld, A., 2012. Rolling friction as a technique for modelling particle shape in DEM. Powder Technol. 217, 409–417.
Wu, K., Yang, D., Wright, N., 2016. A coupled SPH-DEM model for fluid-structure interaction problems with free-surface flow and structural failure. Comput. Struct. 177, 141–161.
Xu, C., Huang, Z., Yao, Y., 2019a. A wave-flume study of scour at a pile breakwater: solitary waves. Appl. Ocean Res. 82, 89–108.
Xu, W.-J., Dong, X.-Y., Ding, W.-T., 2019b. Analysis of fluid-particle interaction in granular materials using coupled SPH-DEM method. Powder Technol. 353, 459–472.
Yang, J., Low, Y.M., Lee, C.-H., Chiew, Y.-M., 2018. Numerical simulation of scour around a submarine pipeline using computational fluid dynamics and discrete element method. Appl. Math. Model. 55, 400–416.
Yang, Y., Qi, M., Wang, X., Li, J., 2020. Experimental study of scour around pile groups in steady flows. Ocean Eng. 195, 106651.
Yang, Z., Lian, X., Savari, C., Barigou, M., 2024. Evaluating the effectiveness of CFD-DEM and SPH-DEM for complex pipe flow simulations with and without particles. Chem. Eng. Sci. 288, 119788.
Yao, W., An, H., Draper, S., Cheng, L., Harris, J.M., 2018. Experimental investigation of local scour around submerged piles in steady current. Coast. Eng. 142, 27–41.
Ye, T., Pan, D., Huang, C., Liu, M., 2019. Smoothed particle hydrodynamics (SPH) for complex fluid flows: recent developments in methodology and applications. Phys. Fluids 31 (1).
Zandi, R., Najafzadeh, M., Lari, K., Ghazanfari-Moghaddam, M.S., 2024. Finding the best shape of floating wave energy converters for different primary geometries: experimental and numerical investigations. Ocean Eng. 307.
Zhang, S., Li, B., Ma, H., 2023. Numerical investigation of scour around the monopile using CFD-DEM coupling method. Coast. Eng. 183, 104334.
Zheng, Z., Hu, Z., Xie, X., Huang, W., 2024. Local scour around the monopile: a microscopic perspective using CFD-DEM. Ocean Eng. 299, 117318.